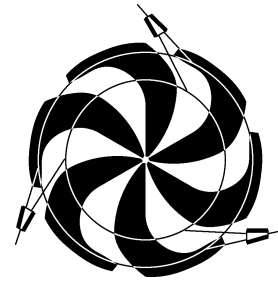# TRIUMF

ANNUAL REPORT
SCIENTIFIC ACTIVITIES
2004

**CANADA'S NATIONAL LABORATORY
FOR PARTICLE AND NUCLEAR PHYSICS**

OPERATED AS A JOINT VENTURE

MEMBERS:

THE UNIVERSITY OF ALBERTA
THE UNIVERSITY OF BRITISH COLUMBIA
CARLETON UNIVERSITY
SIMON FRASER UNIVERSITY
THE UNIVERSITY OF TORONTO
THE UNIVERSITY OF VICTORIA

ASSOCIATE MEMBERS:

THE UNIVERSITY OF GUELPH
THE UNIVERSITY OF MANITOBA
McMASTER UNIVERSITY
L'UNIVERSITÉ DE MONTRÉAL
QUEEN'S UNIVERSITY
THE UNIVERSITY OF REGINA
SAINT MARY'S UNIVERSITY

UNDER A CONTRIBUTION FROM THE
NATIONAL RESEARCH COUNCIL OF CANADA

OCTOBER 2005

PARTICLE PHYSICS

Experiment 614
TWIST – the TRIUMF weak interaction symmetry test
(G. Marshall, TRIUMF)

Normal positive muon decay ($\mu^+ \rightarrow e^+ \nu_e \overline{\nu}_\mu$) is an ideal process to investigate the electroweak interaction in the standard model. The reaction involves only leptons, obviating the need for uncertain strong interaction corrections, thus making it a clean probe of the theory's purely left-handed (V-A) structure. A high-precision determination of the parameters describing the muon decay spectral shape explores physics possibilities beyond the standard model, for example those involving right-handed interactions. The world's most precise such determination has been the goal of Expt. 614, the TRIUMF weak interaction symmetry test (TWIST). The collaboration has recently completed its first phase by directly measuring the muon decay parameters ρ and δ, improving on the accepted Particle Data Group (PDG) [Eidelman *et al.*, Phys. Lett. **B592**, 1 (2004)] values for the two spectral shape parameters by factors of 2.5 for ρ and 2.9 for δ [Musser *et al.* (Phys. Rev. Lett. **94**, in press) TRI-PP-04-21, hep-ex/0409063; Gaponenko *et al.* (Phys. Rev. D, in press) TRI-PP-04-22, hep-ex/0410045].

The four so-called Michel parameters describe the distribution in energy and angle of positrons from polarized muon decay. The spectrum's isotropic part has a momentum dependence determined by ρ plus an additional small term proportional to a second parameter, η. The asymmetry is proportional to a third parameter ξ multiplied by the muon polarization, P_μ, while a fourth parameter, δ, determines its momentum dependence. Within the standard model, the parameters are predicted to be $\rho = 3/4$, $\delta = 3/4$, $\xi = 1$, and $\eta = 0$. These values are shown in Table I along with best experimental measurements prior to the new TWIST results.

Beams of positive muons are used by TWIST since they can be produced with high polarization and high stopping density. The high intensity TRIUMF proton beam produces π^+, some of which decay at rest at the surface of a production target to create a

Table I. Theoretical and measured values of the muon decay parameters.

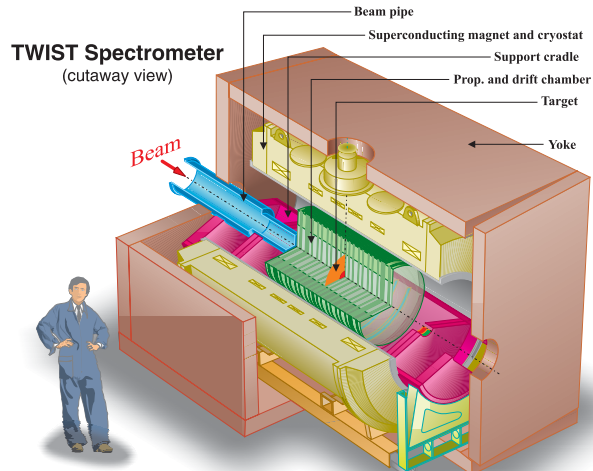|	SM(V-A)	PDG current value
ρ	3/4	0.7518 ± 0.0026
η	0	-0.007 ± 0.013
δ	3/4	$0.7486 \pm 0.0026 \pm 0.0028$
$\mathcal{P}_\mu\xi$	1	$1.0027 \pm 0.0079 \pm 0.0030$

Fig. 1. The TWIST muon-decay spectrometer.

highly polarized "surface" muon beam with momentum $29.6\,\mathrm{MeV}/c$, which is subsequently transported by the M13 beam line into a $2\,\mathrm{T}$ superconducting solenoid. A schematic diagram of the TWIST spectrometer is shown in Fig. 1.

Most of the muon beam stops in a thin target, located at the centre of a symmetric array of 56 low mass, high precision planar drift chambers [Henderson *et al.* (Nucl. Instrum. Methods, in press) TRI-PP-04-20, hep-ex/0409066]. Limitations on final errors are dominated by systematic effects since the statistical precision is very high.

The measured momentum and angle distribution of the decay positrons is shown in Fig. 2. The drop in
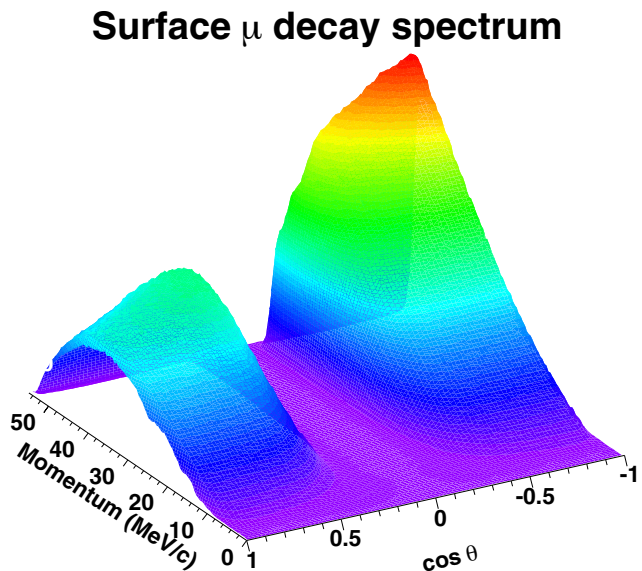

Fig. 2. The observed momentum and angular distribution of positrons from muon decays in the TWIST spectrometer.

acceptance near $|\cos\theta| = 0$ is due to the poor reconstruction efficiency in that region. To extract the muon decay parameters, a two-dimensional fit is made to a fiducial region where the detector acceptance is essentially uniform, utilizing a blind analysis technique. The results are based on 6×10^9 muon decays, spread over sixteen data sets. Four sets were analyzed for both ρ and δ. A fifth set of low polarized muons from pion decays in flight ("cloud" muons) was also analyzed for ρ. The remaining data sets, combined with further MC simulations, were used to estimate the sensitivities to various systematic effects.

TWIST's new measurement of $\rho = 0.75080 \pm 0.00032(\text{stat}) \pm 0.00097(\text{syst}) \pm 0.00023$ (last uncertainty due to the current PDG error in η) sets an upper limit on the mixing angle $|\zeta| < 0.030$ (90% CL) of the W boson with a possible heavier partner W_2 with right-handed coupling. Combining ρ with the new measurement of $\delta = 0.74964 \pm 0.00066(\text{stat}) \pm 0.00112(\text{syst})$, and the PDG value of $P_\mu\xi\delta/\rho$, an indirect limit is set on $P_\mu\xi$: $0.9960 < P_\mu\xi \leq \xi < 1.0040$ (90% CL). The lower limit $0.9960 < P_\mu\xi$ slightly improves the limit on the mass of the heavier boson, $W_2 \geq 420$ GeV/c^2. Finally, an upper limit is found for the muon right-handed coupling probability, $Q_R^\mu < 0.00184$ (90% CL).

In parallel with the major effort to analyze and publish the first data from TWIST, additional new data were taken to establish a direct measurement of $P_\mu\xi$. This was made possible following the replacement of the original Mylar muon stopping target by a very high purity aluminum foil of 71 μm thickness, which should minimize muon depolarization in the target after the muon stops. Another source of depolarization is the muon's passage through the fringe field of the spectrometer solenoid. We are continuing to extend our understanding of the field map in this region, and also of the muon beam characteristics upon which the depolarization depends. An essential tool for the latter is a detector which measures the position and angle of each muon's track by transverse drift in a very low density gas. This device, know as a TEC (time expansion chamber), operates in the beam line vacuum with DME gas at a pressure of 60 torr, contained in a gas box with entrance and exit windows of 6 μm mylar, so as to introduce very little scattering to the low momentum muon beam. The TEC consists of modules (see Fig. 3) to measure tracks in both vertical and horizontal directions, each with up to 24 points, to determine precisely both the location and direction of each muon.

A significant effort is continuing to improve the precision of the analysis software in preparation for final TWIST data, which should become available over the next two years.
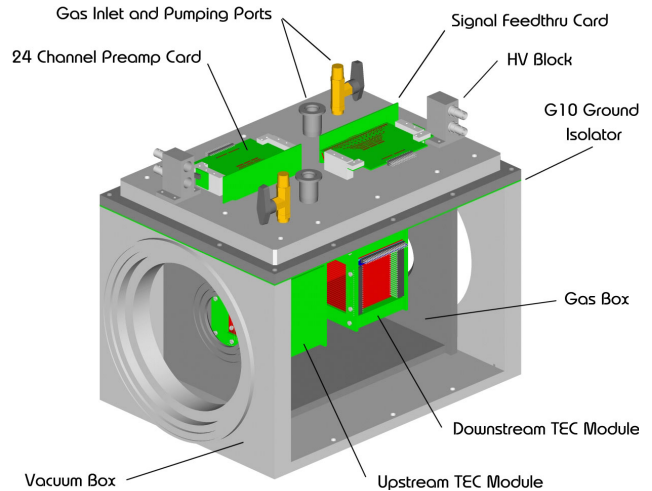

Fig. 3. The TEC, a device which provides characterizations and allows optimization of surface muon beams.

The ATLAS Experiment at the LHC
(C. Oram, TRIUMF)

As described in detail in the 1996 Annual Report, ATLAS is building a general purpose pp detector which is designed to exploit the full discovery potential of the Large Hadron Collider (LHC) at CERN. The TRIUMF group is responsible for the management and engineering of the hadronic endcap (HEC) calorimeters, and the feedthroughs for the endcap cryostats. For the HEC, this year has seen the insertion of the two wheels of the second (and final) endcap into their cryostat (see Fig. 4), and the successful cold test of the first endcap. Final engineering for the transport of the 300 ton endcap cryostats from the assembly hall to the ATLAS pit is under way. The team at CERN responsible for the insertion of the wheels into the cryostats and the cryostat transport is led by a TRIUMF staff member.

Physics goals

The present theoretical understanding of elementary particles is in the context of the standard model. It is a remarkably successful model, providing predictions which have been consistently confirmed by experiments for over two decades. Its agreement with experimental results, to enormous accuracy in some cases, makes it the most accurately verified model in science. Of the many elementary particles contained in the standard model, only the Higgs remains to be discovered. The central goal of ATLAS is the search for the Higgs particle.

There are good theoretical reasons to believe that the discovery of the Higgs will at least contain hints of, and more likely direct evidence for, what lies beyond the standard model. If the Higgs is composite, its existence requires as yet unknown ultra-strong forces. If it is elementary, it would be the only spinless particle
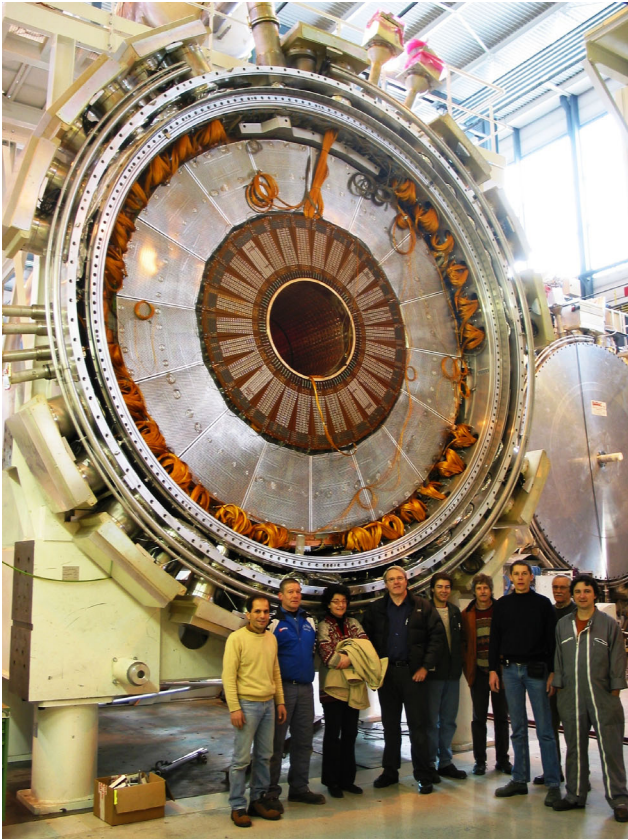
Fig. 4. The second and final cryostat immediately prior to final closure with the cold cover.

to be discovered so far. There is a theoretical "naturalness" problem for the masses of spinless particles. In the standard model, which is a highly nonlinear dynamical system, the elementary particles tend to take on the heaviest of all possible mass scales, which in such a model are at inaccessible energies and inconsistent with other requirements of the model. All other particles discovered thus far have natural mechanisms, such as gauge and chiral symmetries, for protecting their masses so that they can lie in the observable range. For the Higgs particle, there is no such symmetry in the present model. The only theoretical scenarios which leave the Higgs particle light enough to be observed are hypothetical ones, either technicolour or supersymmetry, both radical departures from the present structure of the standard model. If the Higgs is observed at the LHC, one of these scenarios should be seen at the same time.

Particle theory has progressed enormously over the last few decades with many appealing scenarios for physics beyond the standard model. The most likely of these is supersymmetry and the boldest of these is superstring theory. These theories are intimately related and are both radical ideas which promise a new conceptual framework for understanding elementary particles. Though far from being complete theories at present,

there are superstring models which resemble the standard model in their low energy limit. These models have a great appeal as they contain a unification of fundamental forces which includes gravity. They have already had substantial impact on gravitational physics where, for example, in addition to the long sought reconciliation of gravity with quantum mechanics, they have been used to derive a fundamental understanding of black hole thermodynamics. Superstring theory is still in its infancy, but progress has been dramatic and the promise of great things to come has captured the imagination of a substantial fraction of the world's theoretical particle physicists.

The present theoretical view is that the conventional grand unification of the strong, weak and electromagnetic forces can only work in the supersymmetric extension of the standard model. In that model, the grand unified energy scale is only two decades below the Planck scale, the ultimate energy where space-time itself has quantum fluctuations. It is not out of the realm of imagination that, at energy scales where supersymmetry would be observed, evidence for an ultimate theory of everything, or at least everything that can exist once space-time is formed, is within human grasp.

Experiments at the LHC, where the ATLAS detector will take data, will probe the energy region where the Higgs particle and possibly supersymmetry or other structures will be visible. This will be the first experimental probe in many years of an energy region where fundamentally new physics is expected to occur. There is every reason to believe that the results will be among the most dramatic ever.

Basic ATLAS design considerations

The most prominent issue for the LHC is the quest for the origin of the spontaneous symmetry-breaking mechanism in the electroweak sector of the standard model. This is related to one of the most fundamental questions of physics: What is the origin of the different particle masses? New direct experimental insight is required to answer this question.

One of the possible manifestations of the spontaneous symmetry-breaking mechanism could be the existence of a standard model Higgs boson (H), or of a family of Higgs particles ($H^\pm$, h, H and A) when considering the minimal supersymmetric extension of the standard model (MSSM). The Higgs search is therefore used as a first benchmark for the detector optimization. For the SM Higgs, the detector has to be sensitive to the following processes ($\ell = e$ or μ) in order to cover the full mass range above the discovery limit set by the final LEP operation in the fall of 2000:

$H \to b\bar{b}$ from WH, ZH and $t\bar{t}H$ using a $\ell^\pm$ and b-tagging,
mass range $80 < m_H < 100$ GeV;

$H \to \gamma\gamma$
mass range $90 < m_H < 150$ GeV;

$H \to WW^* \to \ell^\pm\nu\ell^\pm\nu$
mass range $150 < m_H < 200$ GeV;

$H \to ZZ^* \to 4\ell^\pm$
mass range 130 GeV $< m_H < 2m_Z$;

$H \to ZZ \to 4\ell^\pm, 2l^\pm + 2\nu$
mass range $m_H > 2m_Z$;

$H \to WW, ZZ \to l^\pm\nu + 2$ jets, $2\ell^\pm + 2$ jets from WW, ZZ fusion using tagging of forward jets for m_H up to about 1 TeV.

In addition to signatures similar to these, the MSSM Higgs searches also require sensitivity to processes such as:

$$A \to \tau^+\tau^- \quad \to e\mu + \nu\text{'s}$$
$$\to \ell^\pm + \text{hadrons} + \nu\text{'s};$$
$$H^\pm \to \tau^\pm\nu \quad \text{from } t\bar{t} \to H^\pm W^\mp b\bar{b} \text{ and}$$
$$\to 2 \text{ jets} \quad \text{using a } \ell^\pm \text{ tag and } b\text{-tagging}.$$

The observable cross sections for most of these processes are small over a large part of the mass range to be explored at the LHC. Hence it is important to operate at high luminosity, and to maximize the detectable rates above backgrounds by high-resolution measurements of electrons, photons, and muons.

Figure 5 shows the estimated signal significance for the standard model Higgs discovery in ATLAS over the presently theoretically favoured region: 100–200 GeV/c^2. From 100–190 GeV/c^2, the most significant discovery channels are those where the Higgs is produced by vector boson fusion [see Asai *et al.*, *Prospects for the search for a standard model Higgs boson in ATLAS using vector boson fusion*, ATLAS Note SN-ATLAS-2003-24]. While the production cross section is lower in these channels, the ability to cleanly tag the Higgs production using forward jets that enter the endcap calorimeters more than compensates, yielding superior signal to noise. The need to use the endcap calorimeters for this tag puts a premium on obtaining an early robust calibration for the calorimeters over the entire angular range.

Canada's participation in ATLAS

The Canadian group consists of about 35 grant eligible physicists from TRIUMF, University of Alberta, Carleton University, Simon Fraser University, University of British Columbia, Université de Montréal, University of Toronto, University of Victoria, McGill University, and York University. We have been strongly
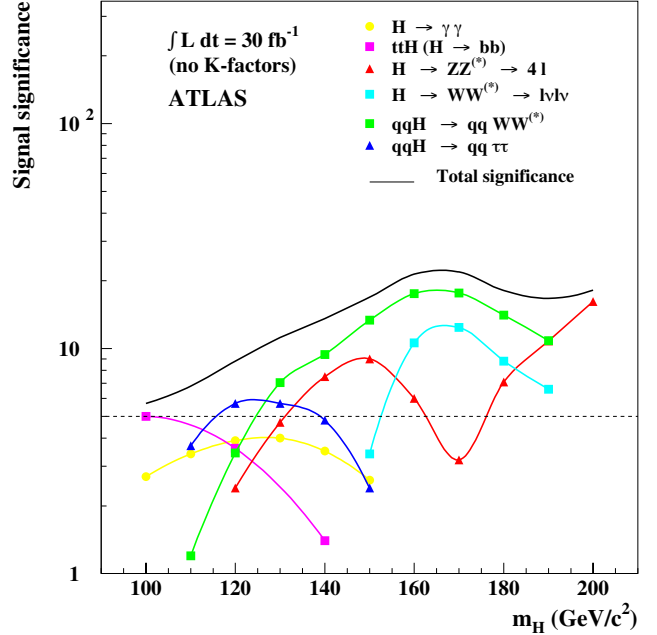

Fig. 5. ATLAS sensitivity for the discovery of a standard model Higgs boson for an integrated luminosity of $30\,\text{fb}^{-1}$. The signal significances are plotted for individual channels, as well as for the combination of all channels.

involved in three construction projects centred around detecting hadrons in the endcap region: the hadronic endcap project, the hadronic portion of the forward calorimeter project, and the pipeline electronics for calorimetry. In addition, as part of our common project contribution, we delivered the cryogenic signal feedthroughs for the two liquid argon endcap cryostats. The calorimeter projects are currently in the final stages of installation. TRIUMF has been directly involved in all of these projects, and is also centrally involved in the detector control system (DCS) for the liquid argon calorimeters. This year Chris Oram was elected to be the ATLAS Collaboration Board (deputy) chair (see the ATLAS organization chart at http://atlas.web.cern.ch/Atlas/-Management/Organization.gif). This appointment is for four years, and makes him deputy chair in 2005, chair in 2006/7, and then deputy chair again in 2008. He sits *ex officio* on the ATLAS executive board for these four years.

The hadronic endcap project

The hadronic endcap (HEC) calorimeter is a liquid argon sampling calorimeter with copper absorbers [ATLAS Collab., ATLAS Liquid Argon Technical Design Report (1996)]. A concise overview of this design was provided in the 1996 TRIUMF Annual Report. An artist's impression of a module can be seen in Fig. 6. Four detector systems sit in each endcap
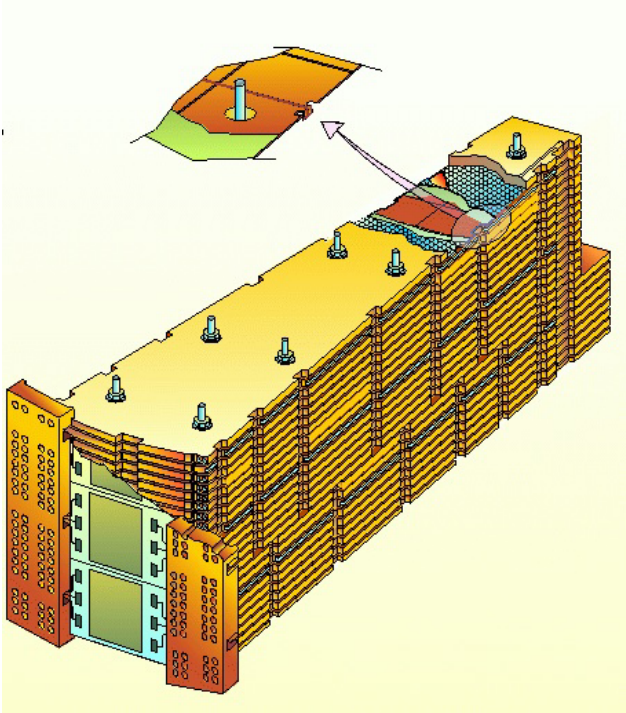
Fig. 6. Artist's impression of a hadronic endcap module.

cryostat: the presampler is closest to the interaction region and is followed by the electromagnetic endcap calorimeter (EMEC) and the HEC. At the inner diameter, the forward calorimeter (FCAL) is installed around the beam pipe.

Hadronic endcap module production and testing As described in last year's Annual Report, all modules have been manufactured and individually cold tested. This year the first endcap, predominately assembled with Canadian modules, was successfully cold tested, essentially bringing to an end this era of construction and testing of equipment.

ATLAS endcap signal feedthroughs The TRIUMF group contributes to the production of high density cryogenic signal feedthroughs for both endcap cryostats. The feedthroughs are critical to the success of ATLAS. They have been built and tested at the University of Victoria by TRIUMF and Victoria staff. The last shipment to CERN took place in January, 2003. The endcap signal feedthroughs have been installed on the two endcap cryostats between December, 2002 and September, 2003. Cabling and tests were finalized in October, 2003, with no failures out of 96,000 electrical channels. Tasks accomplished in 2004 included finalizing the inventory, the storage of spare parts, and the decommissioning of the feedthrough production equipment. The interfacing of component details and electrical test results with the ATLAS database is nearly complete. Readiness for some repairs is being main-

tained until the endcap cryostats are in operation in the ATLAS cavern. A paper describing the ATLAS LAr signal feedthroughs has been written in collaboration with colleagues from Brookhaven National Laboratory (who produced the barrel signal feedthroughs), and has been accepted for publication in Review of Scientific Instruments.

Test beam measurements of the hadronic endcap modules This year we undertook the joint test of the three calorimeters in the endcap. An engineering run of the test beam set-up was undertaken in February, 2004, with beam runs in the spring and fall of 2004. This test of the EMEC, HEC and FCAL was successful, and preliminary results are in agreement with expectations. In addition, it was a full test of the hardware, electronics and software associated with the calorimeter. As such it was a first test of the complete system, and provided a useful pre-test for the up-coming commissioning and initial data-taking era.

BNL 787/949/KOPIO
Measurement of $K \rightarrow \pi\nu\bar{\nu}$ and other rare decays
(D. Bryman, UBC)

The rare decays of K and B mesons play an important role in the search for the underlying mechanism of flavour dynamics and in particular in the search for the origin of CP violation. Among the many K and B decays, the rare decays $K^+ \rightarrow \pi^+\nu\bar{\nu}$ and $K^0_L \rightarrow \pi^0\nu\bar{\nu}$ are very special because their branching ratios can be computed to an exceptionally high degree of precision, not matched by any other flavour-changing neutral-current (FCNC) process involving quarks. While the theoretical uncertainties in the branching ratios of other prominent FCNC processes are at the level of 10% or larger, the theoretical uncertainty in B($K^0_L \rightarrow \pi^0\nu\bar{\nu}$) is only 1–2%. The non-negligible charm contribution leads to a slightly larger theoretical error in the case of B($K^+ \rightarrow \pi^+\nu\bar{\nu}$): 8%, which may soon be reduced significantly. Remarkably, the clean access to underlying parameters in $K^+ \rightarrow \pi^+\nu\bar{\nu}$ and $K^0_L \rightarrow \pi^0\nu\bar{\nu}$, such as for new CP violating phases, remains available in most extensions to the standard model including many examples of supersymmetry.

Although the $K^0_L \rightarrow \pi^0\nu\bar{\nu}$ reaction is extremely rare with the standard model prediction at B($K^0_L \rightarrow \pi^0\nu\bar{\nu}$) = $(2.9 \pm 0.6) \times 10^{-11}$, the new KOPIO experiment has been designed to observe and study it. KOPIO will have unprecedented sensitivity representing an experimental improvement of a factor of 100,000 over previous measurements. (An experiment is currently under way at KEK aimed to reach B $< 10^{-9}$ which is an order of magnitude above the SM prediction.) With this new technology and remarkable sensi-

tivity, KOPIO has the capability of discovering entirely unanticipated phenomena, of revealing discrepancies in existing theory, or inferring inconsistencies by comparison with B meson experiments. KOPIO builds on the success of the E787/E949 measurements of the decay $K^+ \to \pi^+ \nu \bar{\nu}$ at BNL.

Results from the E949 measurement of $K^+ \to \pi^+ \nu \bar{\nu}$

In 2004, E949 reported new results [Anisimovsky *et al.*, Phys. Rev. Lett. **93**, 031801 (2004) TRI-PP-04-07] from data acquired in 2002 using beams, apparatus, and procedures similar to those of E787. Measurements of charged decay products were made in a 1 T magnetic field using an active target, a central drift chamber, and a cylindrical range stack (RS) of scintillator detectors. Photons were detected in a 4π sr calorimeter. Measurement of $K^+ \to \pi^+ \nu \bar{\nu}$ decay from kaons at rest involved observation of the π^+ in the momentum region $211 < P < 229 \, \text{MeV}/c$ in the absence of other coincident activity. Primary background sources were pions from the two-body decay $K^+ \to \pi^+ \pi^0 (K_{\pi 2})$, muons from $K^+ \to \mu^+ \nu (K_{\mu 2})$ and other decays, pions scattered from the beam, and charge exchange reactions followed by $K^0 \to \pi^+ \ell \nu$, where $\ell = e$ or μ.

Each background source was suppressed by two groups of complementary but independent selection criteria (cuts), and the desired level of background rejection was obtained by adjusting the severity of the cuts. After extensive verification of backgrounds, the total number of background events expected in the signal region was 0.30 ± 0.03.

Examination of the signal region for the new data set yielded one event with $P = 227.3 \pm 2.7$ MeV/c, $R = 39.2 \pm 1.2$ cm (range in equivalent cm of scintillator), and $E = 128.9 \pm 3.6$ MeV. The event (2002A) has all the characteristics of a signal event although its high momentum and low apparent time of $\pi \to \mu$ decay (6.2 ns) indicated a higher probability than the two previously observed (E787) candidate events that it was due to background, particularly $K_{\mu 2}$ decay.

The combined result for the E949 and E787 data is shown in Fig. 7 with the range and kinetic energy of the events surviving all other cuts. The result obtained using a likelihood method described in http://www.kopio.bnl.gov/ was B($K^+ \to \pi^+ \nu \bar{\nu}$) = $1.47^{+1.30}_{-0.89} 10^{-10}$ incorporating the three observed events and their associated weights W given in Table II. This result is consistent with the SM expectation although the central value is nearly twice the prediction. The quoted 68% C.L. interval includes statistical and estimated systematic uncertainties. The estimated systematic uncertainties do not significantly affect the confidence levels. The estimated probability that background alone gave rise to the three observed events (or
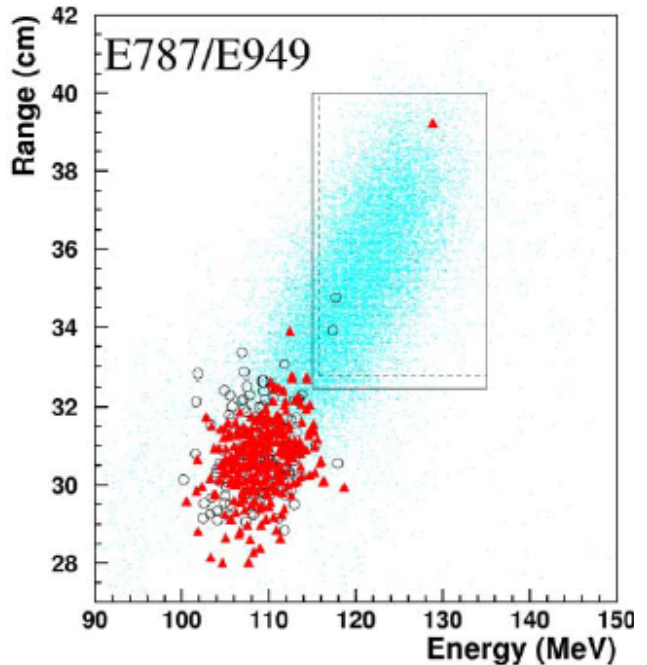

Fig. 7. Range versus energy distribution of events passing all other cuts. The circles represent E787 data and the triangles represent E949 data. The group of events around $E = 108$ MeV was due to the $K^+ \to \pi^+ \pi^0$ background. The simulated distribution of $K^+ \to \pi^+ \nu \bar{\nu}$ events is indicated by dots. The solid line (dashed line) box represents the signal region for E949 (E787).

Table II. Numbers of kaons stopped in the target N_K, total acceptance, total numbers of estimated background events for the E949 and E787 data samples, signal-to-background ratio (S/b) and weight (W) for each observed candidate event calculated from a likelihood analysis, and the estimated probability that the background alone gave rise to each event (or any more signal-like event).

	E787		E949
N_K	5.9×10^{12}		1.8×10^{12}
Total acceptance	0.0020 ± 0.0002		0.0022 ± 0.0002
Total background	0.14 ± 0.05		0.30 ± 0.03
Candidate	1995A	1998C	2002A
S/b	50	7	0.9
W	0.98	0.88	0.48
Background probability	0.006	0.02	0.07

to any more signal-like configuration) was 0.001.

The E787 and E949 data were also used to set a limit on the branching ratio for $K^+ \to \pi^+ X$ where X is a neutral weakly interacting massless particle. The new result was B($K^+ \to \pi^+ X_0$) $< 0.73 \times 10^{-10}$ (90% C.L.), based on the inclusion of event 2002A, which was observed within 2 standard deviations of the expected pion momentum.

Further analysis of E949 data is being pursued vigorously to study the lower energy phase space region ($P < 205\,\mathrm{MeV}/c$) for $K^+ \to \pi^+ \nu \bar{\nu}$ which became accessible due to the E949 upgrade. The potential exists for doubling the sensitivity of E949. In addition, we are using E949 data to study improvements in photon detection efficiency relevant to KOPIO, to search for several non-SM processes (e.g. $\pi^0 \to XX$), and to study several important radiative K decays including $K^+ \to \pi^+ \gamma \gamma$, $K^+ \to \pi^0 \mu^+ \nu \gamma$, and $K^+ \to \pi^+ \pi^0 \gamma$.

History of E949 E949 grew out of the successful precursor experiment, E787, which took data from 1995–98 and improved the sensitivity to $K^+ \to \pi^+ \nu \bar{\nu}$ by four orders of magnitude beyond previous attempts. E787 discovered the first two $K^+ \to \pi^+ \nu \bar{\nu}$ events as well as several other important rare K decays and performed many non-SM searches. E949 was fully operational and poised to collect 10–20 SM-level events when the DOE suspended funding for AGS operations in 2002.

KOPIO

The experimental aspects of measuring $K^+ \to \pi^0 \nu \bar{\nu}$ are challenging. $K^0_L \to \pi^0 \nu \bar{\nu}$ is a three body decay where only the π^0 is observed. There are many competing decays that also yield π^0s but with branching ratios that are billions of times larger. Thus, an approach must be developed with these features: an intense source of K mesons, a detector with maximum possible redundancy for observing the kinematically unconstrained decay, a capability for ensuring that the π^0 is the only observable particle emanating from the decay, and multiple handles for identifying small backgrounds. It is with these issues in mind that KOPIO, shown in Fig. 8, has been designed. The beam and detectors for KOPIO employ well-established technologies in novel configurations. New aspects have been
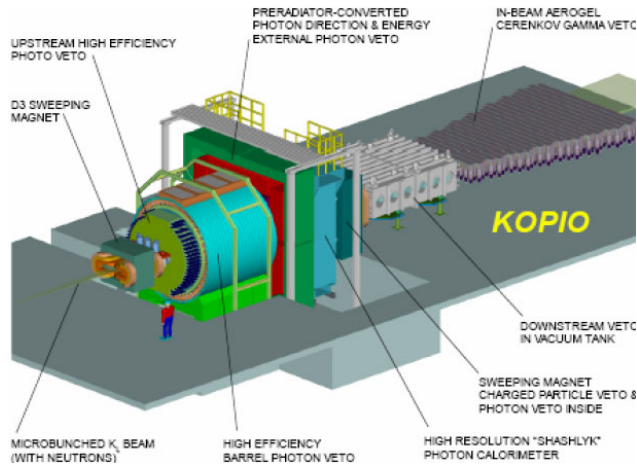

Fig. 8. An engineering perspective of the KOPIO experiment. The apparatus occupies approximately 15 m along the beam line.
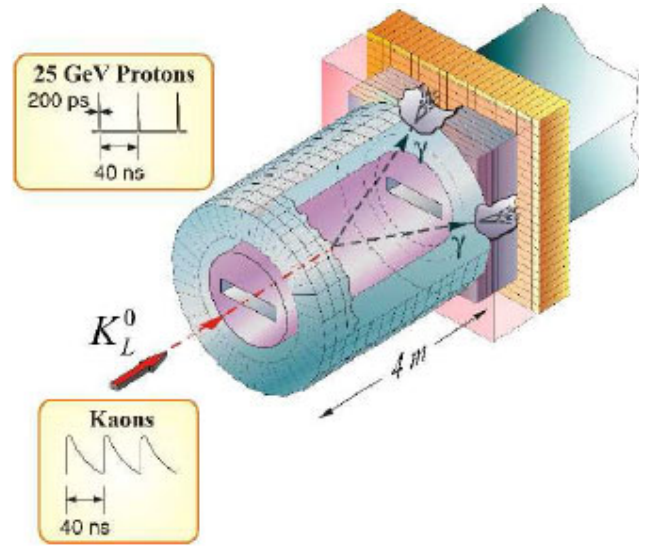

Fig. 9. Schematic of the KOPIO experiment. The time-bunched neutral K meson beam enters from the left. K decays are imaged using the detection of two photons that interact in the preradiator and the calorimeter on the right. The decay region is surrounded by veto detectors.

confirmed in beam measurements, with prototypes, and with simulations.

The concept for KOPIO is shown schematically in Fig. 9. The 24 GeV primary proton beam from the AGS is presented to the production target in 200 ps wide pulses at a rate of 25 MHz. A 360 μsr solid angle neutral beam is extracted at 42.5° to produce a "soft" K^0_L spectrum peaked at 0.65 GeV/c. The low energy, time-structured neutral beam allows determination of the incident K^0_L momentum using the time-of-flight technique. The vertical acceptance of the beam (4 mrad) is kept much smaller than the horizontal acceptance (90 mrad) so that effective collimation can be applied to severely limit neutron halos and to obtain another constraint on the decay vertex position. Downstream of the final beam collimator is a 4 m long decay region which is surrounded by the main detector. The beam region is evacuated to a level of 10^{-7} torr to suppress neutron-induced pion production. The decay region is surrounded by an efficient charged particle veto detector and Pb/scintillator photon veto detector.

The detection system for $\pi^0 \to \gamma \gamma$ decay allows a fully constrained reconstruction of the decay vertex, and mass, energy, and momentum measurements in the K^0_L centre of mass system. This is accomplished by measuring the position of interaction, angle, and energy of each individual photon in a fine grained preradiator (PR) detector followed by an efficient calorimeter.

The PR is a high resolution, high efficiency γ-ray imaging device under development at TRIUMF. Using an array of plastic scintillation counters and dual coor-

dinate drift chambers, the PR will accurately measure positions, energies and angles of photons in the range of 50 to 500 MeV. The resolutions expected are $250\,\mu$m, $\frac{3\%}{\sqrt{E(\text{GeV})}}$, and 25 mrad, for position, energy and angle (at 250 MeV), respectively, based on KOPIO prototype and other measurements and simulations. Efficiency of detection for photons in the preradiator is expected to be 70%.

The goal of the KOPIO experiment is to explore new physics such as CP-violating phases with a sensitivity equivalent to measuring 100 standard model events. The present plan calls for running of the experiment to commence in 2011 with three years of data acquisition. In addition to the $K_L^0 \rightarrow \pi^0\nu\bar{\nu}$ decay, many other radiative type K decays of significant interest and searches for non-SM processes will also be accessed simultaneously. At the conclusion of the KOPIO experiment, either the SM picture of CPV will be shown to be consistent with present knowledge and the relevant parameters measured accurately, or a new approach to understanding quark mixing and CP violation will have been shown to be required.

The preradiator

The preradiator (PR) is at the heart of the KOPIO signal detection technique designed to efficiently measure the position, angle, time, and energy of photons. The PR will be arranged in four quadrants of modules shown in Figs. 10 and 11. A module consists of eight
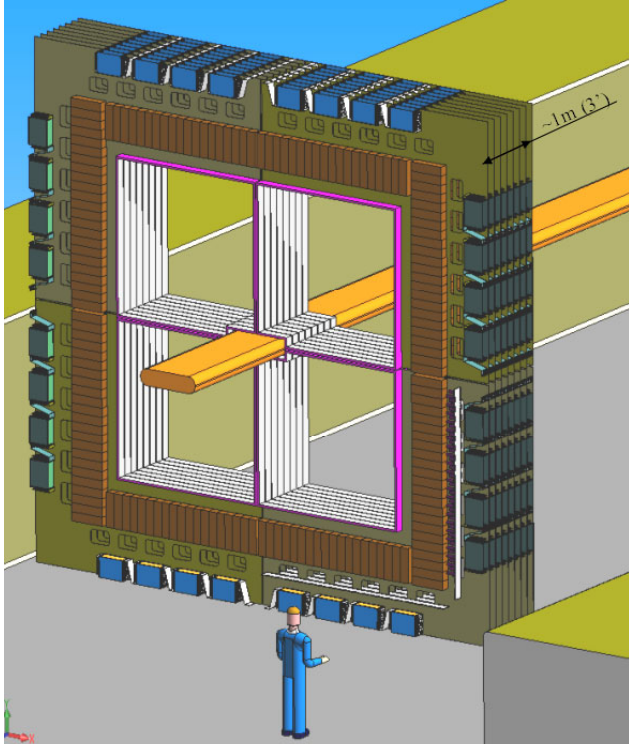
1.5 m $\times$ 1.5 m drift chambers and 9 scintillator sheets.

Preradiator R&D

Drift chambers Several stages of prototype chambers have been constructed to verify the position resolution and develop compatible electronics. A stack of five chambers was used to measure the position resolution of cathode strip arrangements. The resolution for a chamber with 5 mm wide strips was $\sigma = 213 \pm 14\,\mu$m, compatible with the requirements, and anode-wire position resolution $\sigma = 199 \pm 14\,\mu$m was obtained. There was no drift time dependence to the resolutions indicating that contributions such as misalignment dominated. Further cathode resolution tests accommodating larger angles up to 45° are being carried out and two full length test chambers, with 2 m long anode wires (short strips – see Fig. 12), and with 2 m long cathode strips (short wires), were constructed and have been used for the development of front-end electronics to study efficiency, timing distributions, pulse shape variations, and other parameters. Signal characteristics as a function of position, signal-to-noise ratios, and efficiencies are being studied and modelled.

Prototypes of the KOPIO anode and cathode read-out cards were also manufactured and tested. Each channel is composed of an amplifier and level adaptor.

Fig. 10. PR detector composed of 32 modules organized in 4 quadrants of 8 modules surrounding the beam pipe.
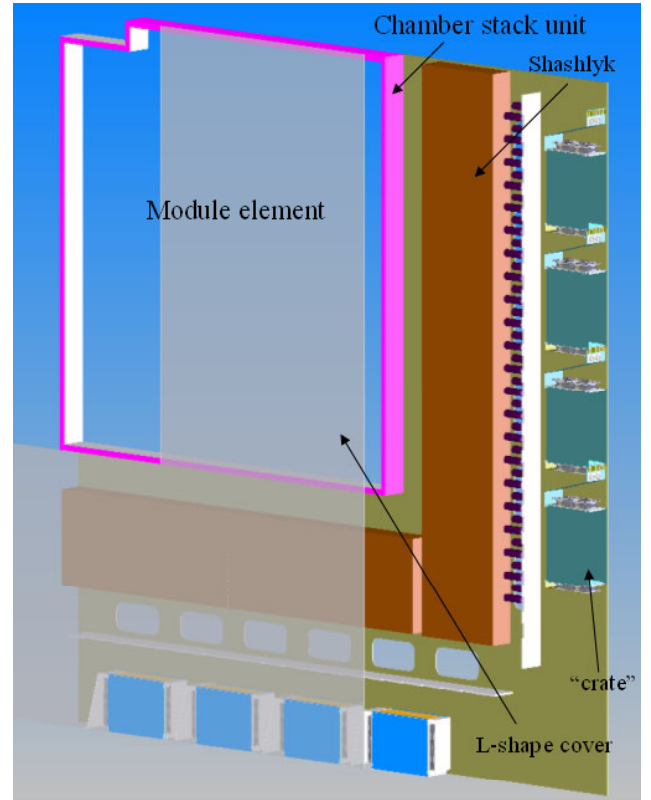

Fig. 11. Module with the chamber stack (pink), Shashlyk (red), and electronic crates (blue).

Fig. 12. 2 m long anode wires with short strips.

For the cathodes, six octal flash ADCs sample the signals and deliver the digital data to their corresponding FPGAs for data processing. The eight channels of each flash ADC are processed in the associated FPGA and sent through a single LVDS output to another FPGA for data merging and data transmission. Self-triggering or an external trigger can be selected in each mode of operation: time window mode, time offset mode, and algorithm mode. Forty prototype cathode readout cards will be assembled and used in the full scale KOPIO PR module prototype set-up. Anode cards consist of front end amplifier-discriminators followed by pipeline TDCs and FPGAs.

Scintillator studies During the past two years we have been perfecting the production of extruded polystyrene scintillator in conjunction with a local company, CELCO Industries (Surrey, BC). The extrusions have dimensions $1\,\text{cm} \times 7\,\text{cm} \times 2.5\,\text{m}$ with six $1\,\text{mm}$ holes for WLS fibres. A recent product is shown in Fig. 13. After achieving the dimensional and flatness tolerances and hole extrusion techniques, we studied properties including light output, attenuation, and hole dimensional tolerance. The tests indicate that the amount of the scintillation light from the extruded scintillator was comparable to that of St. Gobain commercial scintillator BC408, though the measured $15\,\text{cm}$ attenuation length affected the yield of photo-electrons via WLS readout; the quality of the extruded hole did not have much impact on the photo-electron yield; and MC calculations reasonably describe the WLS readout. To match the precision required for the PR module construction, the extrusions will be machined with tongue and groove on the edges for gluing into $1.5\,\text{m} \times 1.5\,\text{m}$ sheets using a gluing jig. The first thirty-five satisfactory planks were produced in September.
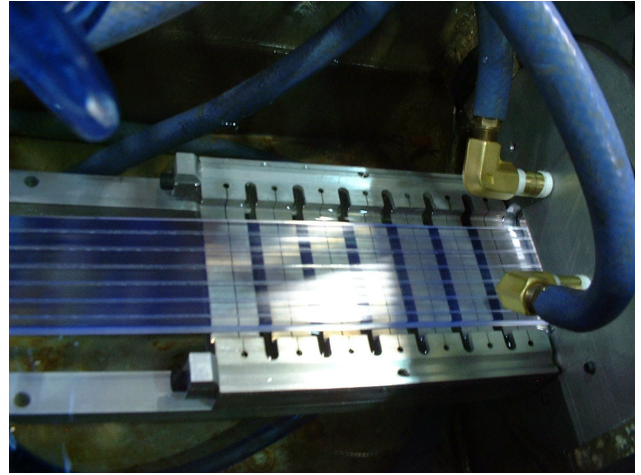

Fig. 13. Scintillator during extrusion process.

After basic tests on the extruded scintillators, the test set-up was modified to accommodate five scintillator pieces, each with six $1\,\text{mm}$ diameter holes for WLS fibres which were bundled and read out by a Hamamatsu 3178X photo-multiplier from one end. Using an $X - Y$ readout drift chamber, data were taken simultaneously for the five scintillators and for position dependence across the scintillator. The average number of photo-electrons was 8 p.e./MeV per end with a slight (10%) dependence on the coating/wrapping material. This statistically corresponds to $\sigma_E = \frac{1\%}{\sqrt{\text{E(GeV)}}}$ energy resolution and we expect to read out both ends. The observed time resolution of approximately 2 ns corresponds to $\sigma_t = \frac{120\,\text{ps}}{\sqrt{\text{E(GeV)}}}$ for minimum ionizing particles. Both resolutions conform to KOPIO requirements and are expected to be improved.

KOPIO neutral beam design work at TRIUMF

The neutral K_L^0 beam line is a system of collimators that defines a highly asymmetric beam. During 2004, many studies were made at TRIUMF including investigation of the optimal aspect ratio where a better halo was obtained; minimizing the length of the beam without substantially increasing the neutron halo; reducing the thickness of the photon attenuator to increase the K flux; using a magnetic field in the last collimator to reduce the charged kaon contamination to 10^{-7} of the neutral beam; adding another collimator to limit the entrance aperture just before the decay region to decrease the neutron halo by a factor of 2; and, studies of the material of the collimators which showed that W is best. Our conclusion is that the many aspects of the beam are now well understood.

AGS upgrade work for KOPIO at TRIUMF

The AGS will be upgraded for KOPIO to provide higher beam intensity with a significantly mod-

ified time structure. Three upgrades to the AGS are planned: (1) extraction of a micro-bunched proton beam; (2) increasing the proton intensity by a factor of 1.5 or more to 10^{14} protons (100 Tp) per AGS cycle; and (3) constructing a new proton beam line to bring the intense micro-bunched beam to a new K meson production target. The TRIUMF/UBC team was awarded a CFI International Access grant for the Canadian portion of this work, contingent on NSF funding of the KOPIO experiment in the US. In 2004, the CFI provided initial funds for advanced planning to initiate the R&D effort to meet the Canadian responsibilities for items (1) and (2) while the NSF provided funds for items (1)–(3). This work will allow the designs and specifications for these upgrades to be advanced to the point where detailed design, fabrication and placement of contracts can be initiated. Ewart Blackmore (TRIUMF) is coordinating the Canadian AGS upgrade efforts.

25 MHz microbunching cavity The specifications for the 25 MHz microbunching cavity to be provided by TRIUMF include a cavity centre frequency of 24.8694 MHz (67$^{\text{th}}$ harmonic of revolution frequency) and a gap voltage of 150 kV. The RHIC 28 MHz cavity design is to be used for reference. The R&D work also involves simulations of the cavity using the HFSS radio frequency design code in order to study the resonant frequency, tuning and coupling to the amplifier. A full-scale 3D model of the 25 MHz cavity will be fabricated for low power rf tests and optimization.

AGS injection kicker Two new kicker modules will be installed in the AGS ring to add to the existing kicker strength in order to provide the 3 mrad deflection required for 2 GeV protons into the AGS. The TRIUMF group has proposed a new design of transmission line kicker to accomplish this task. Detailed specifications have been developed. Proposed prototype work includes computer modelling to gain a good understanding of the performance of the kicker system. In addition, we will design and test a prototype transmission line type kicker.

The HERMES Experiment
(C.A. Miller, S. Yen, TRIUMF)

Introduction

The HERMES experiment was designed to comprehensively study the spin structure of the nucleon. It has been running at the 27.5 GeV HERA electron accelerator at the DESY Laboratory in Hamburg, Germany since 1995, measuring spin asymmetries for deeply inelastic electron scattering (DIS) as well as a wealth of unpolarized observables. The combination of a polarized high energy electron beam in a storage ring with undiluted polarized atomic gas targets is unique in

this field, and has important experimental advantages. Furthermore, the spectrometer detecting the scattered electrons has substantial acceptance and the capability to identify all types of hadrons produced in coincidence.

This was a very productive year of running at HERA while HERMES continued to accumulate data with a transversely polarized hydrogen target. As was explained in some detail in last year's Annual Report, the asymmetries for the semi-inclusive deep-inelastic events found in these data are sensitive to the previously unmeasured transversity quark distribution. This sensitivity arises through a feature of the fragmentation process described by the Collins function. It acts as a "quark polarimeter" through the appearance of an asymmetry in the distribution of produced pions in the azimuthal angle about the virtual photon direction with respect to the linear polarization of the virtual photon in the lepton scattering plane. Such data from the 2002/03 running years were the basis for a Physics Review Letter, which was published in 2004. Because of the much improved performance of the accelerator, the 2004 running added about three times as much again. Results from these new data will be released in 2005. Running with transverse target polarization will continue until late 2005.

While the new data accumulates, the collaboration continued to complete analyses of the data of previous years, release new preliminary results and publish final ones. Space permits only some highlights to be mentioned here. One publication in Physics Review D was a detailed account of the extraction of quark helicity distributions from the measurements of semi-inclusive deep-inelastic scattering with longitudinally polarized hydrogen and deuterium targets in 1996–2000. The polarizations of the three light flavours of sea quarks are independently determined. This fulfills one of the main original goals of the experiment.

Deeply virtual Compton scattering

One of the dramatic developments of the last decade in the field of nucleon spin physics is the emergence of hard exclusive production of photons and mesons as a new window on nucleon spin structure. New factorization theorems relate observables in such processes to generalized parton distributions (GPDs), which encode both the contribution of parton orbital angular momenta to the nucleon spin, as well as the correlation between the longitudinal momentum of partons and their transverse position. This year, HERMES released new results for the kinematic dependence of beam-charge asymmetries for the hard exclusive deeply virtual Compton scattering (DVCS) process on the hydrogen and deuterium targets. Figure 14 shows their dependence on the momentum transferred
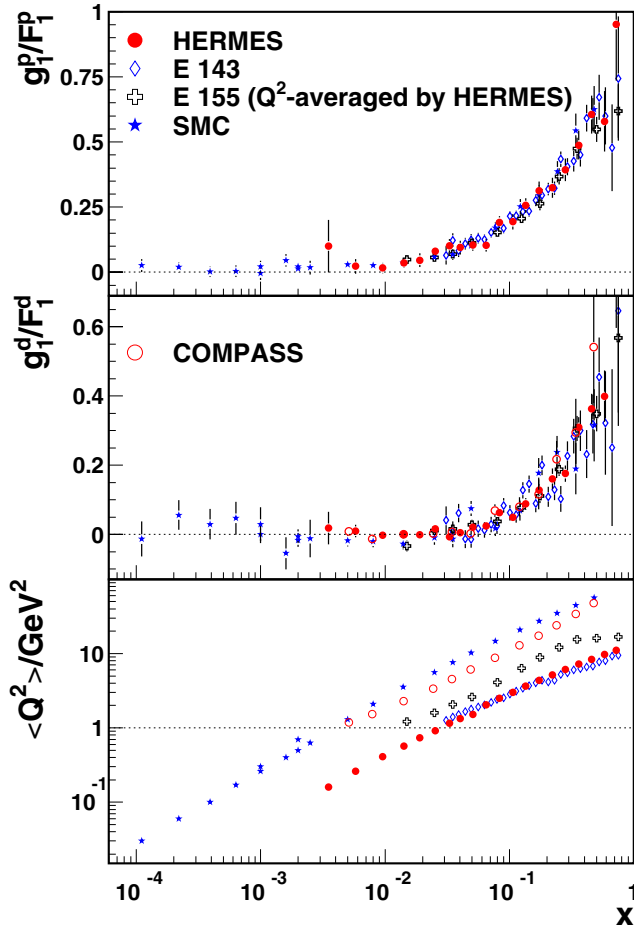
Fig. 14. The virtual-photon asymmetry $g_1(x)/F_1(x)$ for the proton and the deuteron, compared to world data, each at its measured value of Q^2 shown in the lower panel.

to the target nucleon, which remains intact even after one of its quark absorbs a hard virtual photon and then re-emits an energetic real photon. The asymmetries arise from interference with the well-understood Bethe-Heitler process (radiative elastic scattering), giving sensitivity to the DVCS amplitudes. Hence the deuterium asymmetry arises almost entirely from the proton, as the Bethe-Heitler cross section on the neutron is negligible except in the last t-bin. The more precise new deuterium results now confirm the earlier observation on hydrogen of a significant asymmetry at intermediate t-values. These data can be compared to the predictions of various models for GPDs. The asymmetries with respect to transverse target polarization for the events now being recorded from both DVCS and exclusive production of pions will introduce new independent constraints on GPDs.

Interference fragmentation functions

Another new result released this year is the first observation of an asymmetry with respect to longitudinal target polarization in the semi-inclusive production

of $\pi^+\pi^-$ pairs in deep-inelastic scattering. Theoretical predictions of such a possible asymmetry based on an "interference fragmentation function" were motivated by the role it could play as another polarimeter for transverse quark polarization, potentially yielding an independent signal of transversity. An asymmetry did appear in this data, although not with conclusive statistical significance. A larger asymmetry is expected to appear in the data now being recorded with transverse target polarization.

The spin structure function g_1

A primary goal of the HERMES experiment was the precise measurement of the inclusive spin-structure function $g_1(x)$, in deep-inelastic scattering on both hydrogen and deuterium targets. Results for hydrogen were published several years ago. This year, final results for deuterium were also released, together with a reanalysis of the hydrogen data using the refined techniques that have since been developed. These structure functions have been measured in other experiments at both SLAC and CERN. However, the new deuterium data are the most precise available. Furthermore, when all of the available data measured over a significant range in Q^2 representing the hard scale of the process are combined in global analyses, the Q^2-evolution of the structure functions can be extracted. Due to the coupling of quarks and gluons described by QCD, this evolution constrains the polarization of gluons with respect to the nucleon longitudinal spin orientation. The new results for the ratio $g_1(x)/F_1(x)$ of structure function (closely releated to virtual-photon asymmetries) are compared to world data in Fig. 14. This ratio is expected and found to have little dependence on Q^2. The corresponding values of $g_1(x)$ from HERMES are shown in Fig. 15. The HERMES error bars in these plots cannot be compared directly to those of other experiments, as only the HERMES analysis includes full unfolding of the kinematic smearing due to instrumental resolution and QED radiation, which inflates the diagonal elements of the covariance matrix. However, the compensating interbin correlations represented by the negative off-diagonal elements are accounted for in the calculation of first moments of g_1, which are shown in Table III. The statistical precision of the HERMES data on the proton is competitive and on the deuteron it is superior.

Fragmentation

Parton distribution functions are not the only observables relevant to understanding confinement in QCD. Equally important are fragmentation functions that describe how an energetic quark ejected from a hadron in a hard collision becomes incorporated into a new hadron together with quarks found in the

Table III. Comparison of the first moments of the structure function g_1 measured by various experiments with that measured by HERMES, in a common measured x-range in each case. The references in the last column appear in Table IV.

Experiment	Q^2 [GeV^2]	x-range	Target	Moment	Our moment in the same x-range	Reference
HERMES	5	0.021–0.9	p	$0.1246 \pm 0.0032 \pm 0.0074$	–	1
E143	5	0.03–0.8	p	$0.117 \pm 0.003 \pm 0.006$	0.1174 ± 0.0027	2
SMC	5	0.03–0.7	p	0.128 ± 0.006	0.1141 ± 0.0026	2(*)
SMC	10	0.003–0.7	p	$0.131 \pm 0.005 \pm 0.006 \pm 0.004$	(**)	3
HERMES	5	0.021–0.9	d	$0.0452 \pm 0.0015 \pm 0.0017$	–	1
E143	5	0.03–0.8	d	$0.043 \pm 0.003 \pm 0.002$	0.0433 ± 0.0013	2
E155	5	0.01–0.9	d	$0.0408 \pm 0.0025 \pm 0.0024$	(**)	4
SMC	5	0.03–0.7	d	0.043 ± 0.007	0.0416 ± 0.0013	2(*)
SMC	10	0.003–0.7	d	$0.037 \pm 0.006 \pm 0.003 \pm 0.003$	(**)	3
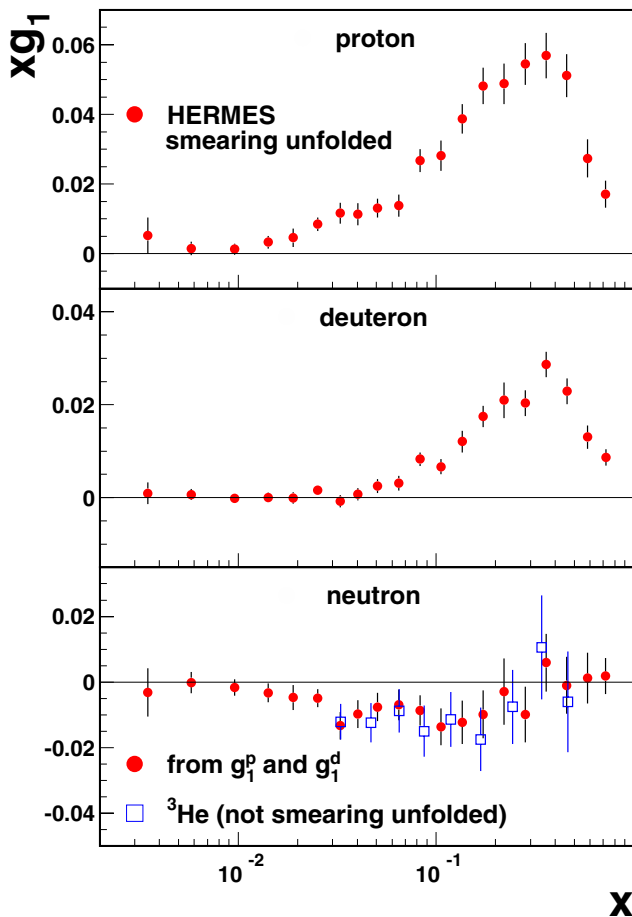
Fig. 15. The spin structure function $g_1(x)$ for the proton and the deuteron.

Table IV. References for the moments shown in Table III.

1	HERMES g_1 paper in preparation
2	E143, Abe *et al.*, Phys. Rev. **D58**, 112003 (1998)
2(*)	Same as above, results calculated by E143 in a smaller x-range than SMC
3	SMC, Adeva *et al.*, Phys. Rev. **D58**, 112001 (1998)
4	E155, Anthony *et al.*, Phys. Lett. **B463**, 339 (1999)
(**)	A comparison value is not calculated because it would mean using our data at $Q^2 < 1$ GeV^2

capability over the full kinematic acceptance. Furthermore, as the HERMES energy regime is lower than collider energies, it is important to compare the results in the two regimes to ensure that they are universal, as expected from factorization theorems.

A fragmentation function represents the number density of hadrons of a particular type that are produced by a struck quark of a particular flavour, expressed as a function of the scaling invariant z. In the target rest frame, z is the hadron energy E_h as a fraction of the energy ν of the virtual photon. The first step towards extracting fragmentation functions is to measure hadron multiplicities for both hydrogen and deuterium targets. New precise multiplicity results for hydrogen were released this year, and are shown as a function of z in Fig. 16. As the contributions from the decay of exclusively produced vector mesons (ρ and ϕ) may not be regarded as a legitimate part of semi-inclusive DIS, results are also shown after their subtraction using simulations tuned to measured exclusive cross sections.

The DIS factorization theorem implies that hadron multiplicities should be independent of x, the momentum fraction of the struck parton in the target. Figure 17 shows the measured multiplicities as a function

vacuum. A wealth of information about fragmentation has been extracted from e^+e^- collider data. However, most of these data are not sensitive to the full flavour dependence of fragmentation. Deep-inelastic scattering on both hydrogen and deuterium targets can provide this sensitivity when complete hadron identification is available. HERMES is equipped with a dual-radiator ring-imaging Čerenkov detector that provides this
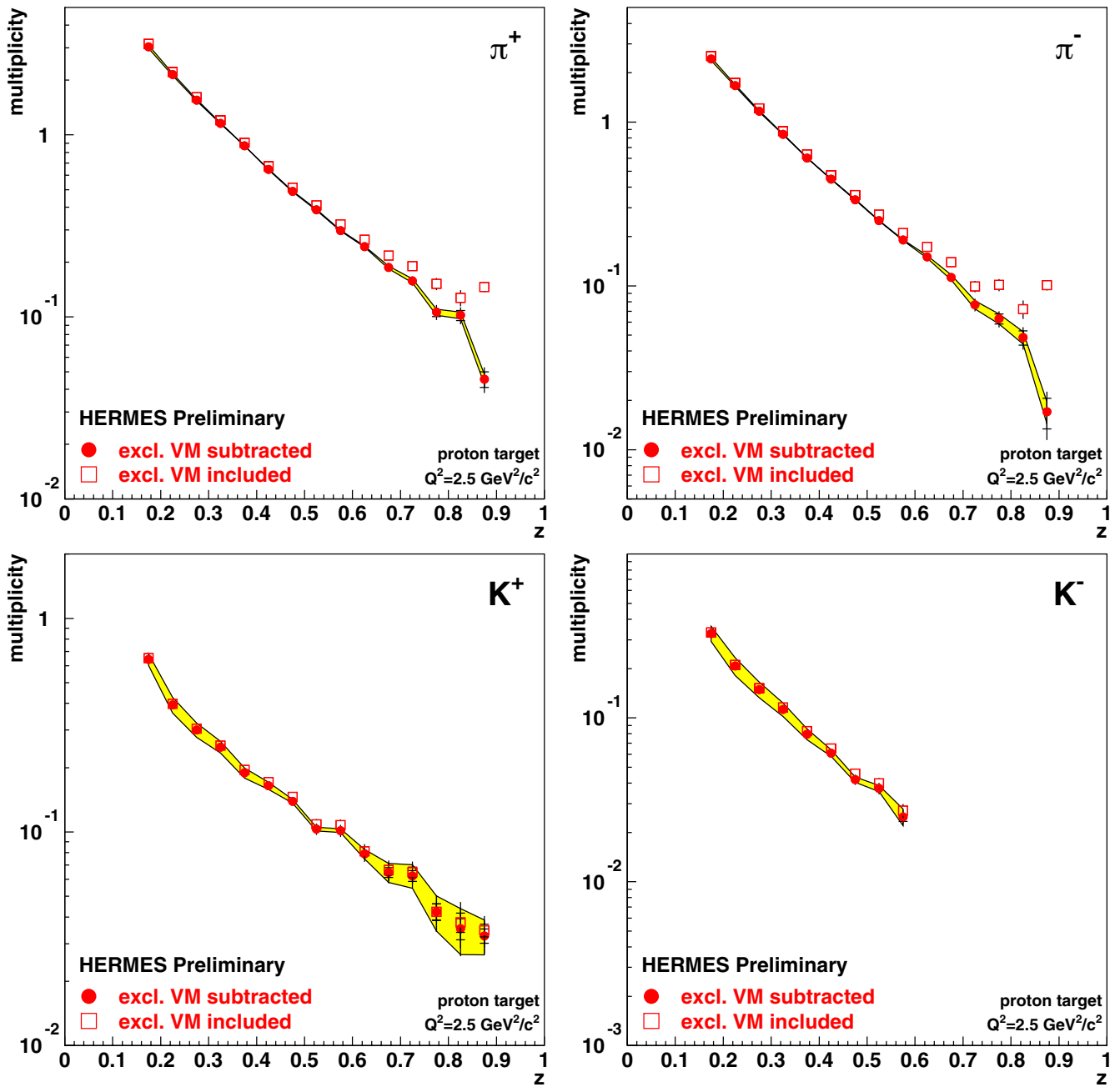
Fig. 16. Hadron multiplicities as a function of z measured by HERMES on the hydrogen target, corrected to 4π acceptance and evolved to a fixed scale $Q^2 = 2.5\,\mathrm{GeV}^2$. The statistical error bars are typically too small to be visible, and the systematic uncertainties are shown as the error bands. Values are shown both with and without subtraction of the simulated contribution from exclusive production of vector mesons.
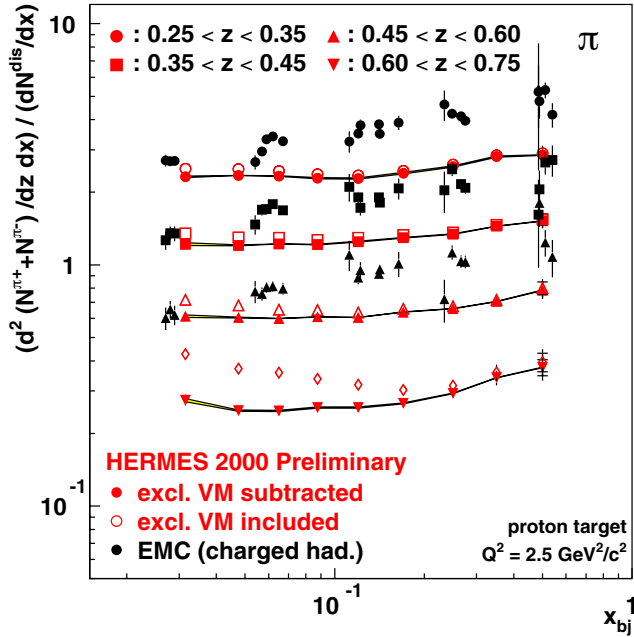
Fig. 17. Charged pion multiplicities as a function of x in four intervals in z, corrected to 4π acceptance and evolved to a fixed scale $Q^2 = 2.5$ GeV^2, as measured by HERMES at 27.57 GeV and by the EMC experiment at CERN at 100–280 GeV [Ashman *et al.*, Z. Phys. **C52**, 361 (1991)]. (The EMC data includes all charged hadrons.)

of x, for several bins in z. They are compared to results from measurements at higher energy at CERN, the x dependence of which has been a long-standing puzzle. The new HERMES results after subtraction of the exclusive "contamination" show little such dependence. Hence the puzzle may be more experimental than theoretical.

When quark fragmentation occurs in the nuclear environment, it becomes possible to study the sequential stages of this process via the dependence of the effects of the nuclear medium on the nuclear size and the kinematics of the process. The understanding of quark propagation in the nuclear medium is crucial for the interpretation of ultrarelativistic heavy ion collisions. Deeply inelastic scattering (DIS) of charged leptons is an ideal tool for this study, as it provides direct measurement of the kinematic properties of the struck quark. It turns out that the ideal range of energy transfer to the struck quark is 10 to 20 GeV, where the hadron formation length is similar to a typical nuclear size. Hence the HERMES experiment at 27.5 GeV beam energy is well placed to pursue these studies. The usual observable of interest is the multiplicity ratio $R_A(\nu, z)$ – the ratio of the DIS hadron multiplicity measured on a target nucleus to that measured on deuterium. In the absence of nuclear effects on fragmentation, this ratio will be unity. An extensive set of precise data for identified pions and kaons, protons and

antiprotons was published by HERMES the previous year [Airapetian *et al.*, Phys. Lett. **B577**, 37 (2003)], giving the dependence of the nuclear ratio on both ν and z. Various theoretical models are able to explain the main features of those data, namely that the ratio decreases as the target mass increases, as ν decreases, or as z increases. These models variously account for energy loss by the energetic struck quark via gluon bremsstrahlung as it propagates through nuclear matter, nuclear absorption of the embryonic colour-singlet "pre-hadron", and/or absorption of the hadron if it is fully formed within the target. These data revealing the effects of cold nuclear matter of moderate density have constrained interpretations in the context of hot dense nuclear matter of the discovery at RHIC of complete suppression of back-to-back jet pairs in central Au+Au collisions, while two-hadron correlations in the same jet survive. One such interpretation is that fragmentation at RHIC is occuring mostly outside the nucleus, and the jet suppression is due to parton energy loss in the medium [Wang, Phys. Lett. **B579**, 299 (2004)]. It was proposed to test this hypothesis by extracting two-hadron attenuation at HERMES. A useful observable here is the super-ratio of the nuclear suppression of two-hadron production to that for one-hadron production:

$$\mathcal{R}_{2h}(z_2) = \frac{\frac{\sum_{z_1 > 0.5} N_A^{(2h)}(z_1, z_2)}{\sum_{z > 0.5} N_A^{(1h)}(z)}}{\frac{\sum_{z_1 > 0.5} N_D^{(2h)}(z_1, z_2)}{\sum_{z > 0.5} N_D^{(1h)}(z)}} \; .$$

If parton energy loss were dominant, then in terms of the Lund string model of fragmentation, this ratio can be expected to be reduced only moderately below unity via the further energy loss by the lower energy remnant quark after the first string break. Most of the gluon radiation is done by the more energetic leading quark. On the other hand, if nuclear absorption of (pre-)hadrons were dominant, then there would be roughly twice as much absorption suppressing two-hadron production.

HERMES has now released the first such measurements of the two-hadron to one-hadron attenuation super-ratio. The results for nitrogen and krypton targets are shown in Fig. 18 as a function of the z_2 value of the slower of the two hadrons, while the leading hadron is required to have a z_1 value greater than $1/2$. The values are indeed only marginally below unity, perhaps somewhat more so for the heavier target. This supports the dominance of energy loss via gluon bremsstrahlung. A recent theoretical calculation of this quantity within such a model is in fair agreement with these nitrogen data [Majumder, nucl-th/0503019]. In this picture, the rise at small values of z_2 can be understood in terms of both small energy loss by the slower quark as well
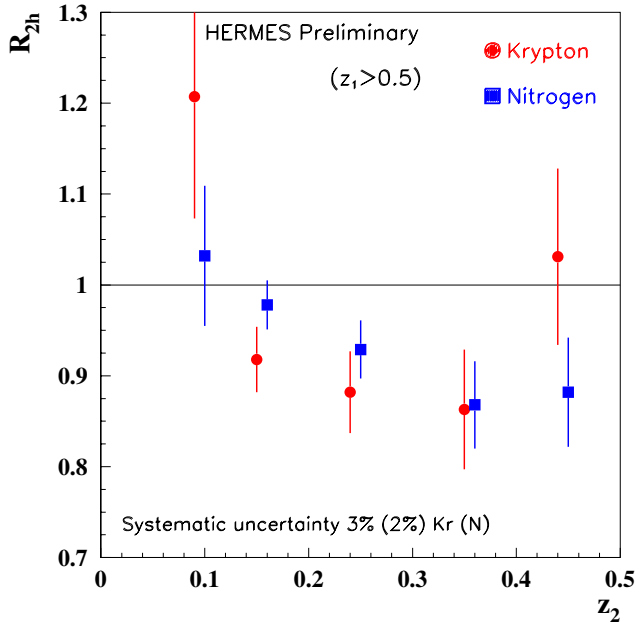
Fig. 18. The super-ratio of the nuclear attenuation of two-hadron production in DIS on nitrogen or krypton to the nuclear attenuation of one-hadron production, as a function of the z_2 value of the slower hadron. The leading hadron is required to have a z_1 value exceeding 1/2.
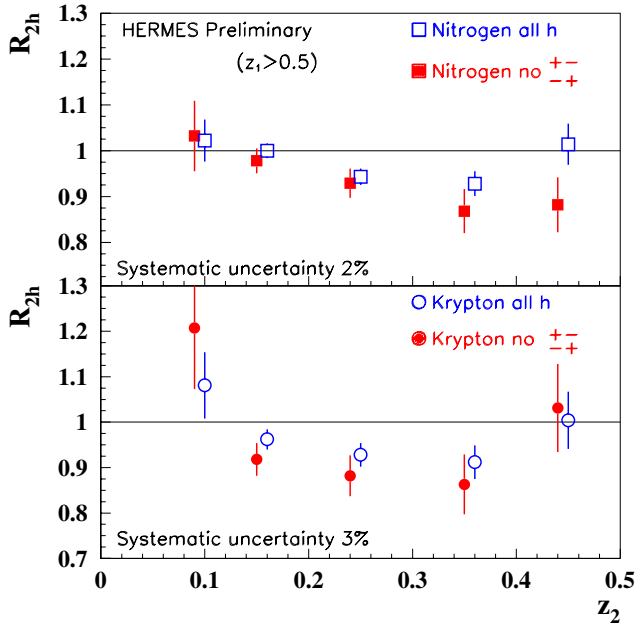

Fig. 19. As in Fig. 18, but additionally the effect of excluding oppositely charged hadrons is shown.

as hadron formation by a radiated gluon. Figure 19 shows the effect of excluding hadron pairs with opposite charge which, in the context of the Lund string model of fragmentation, requires that the two hadrons differ in "rank" by more than unity, i.e. they cannot be separated by only one string-break. (The effect of excluding hadron pairs from decay of exclusively pro-

duced ρ mesons was shown to be negligible by restricting the invariant mass of the pair to not fall near the ρ mass.) The requirement that the slower hadron have a lower rank appears to only slightly suppress two-hadron production. This requirement might be naively expected to increase nuclear absorption of the hadron, as such a hadron will be formed closer to the original interaction point and hence further inside the nucleus. However, detailed model calculations are needed, and can be tested by these data.

The ongoing HERMES program

DESY has promised beam for HERMES until mid-2007. The present running plan is to continue until late 2005 on the transversely-polarized hydrogen target to complete the first measurement of quark transversity in the proton. Meanwhile, HERMES has assembled and is testing a new recoil detector to surround the target cell and detect the recoiling intact target nucleon from hard exclusive processes, in order to guarantee their exclusivity. This detector will be installed in late 2005 and will be the centre-piece for the following two years of running on high density unpolarized targets in 2006/07. This will yield the first really high quality data on asymmetries in both beam spin and charge for DVCS, the process that holds the most promise to shed light on the orbital angular momentum of partons.

HERMES collaborators in 2004: J. Lu, C.A. Miller, S. Yen (TRIUMF), G. Gavrilov (TRIUMF, visiting from DESY), K. Garrow (Alberta/SFU).

J-PARC
T2K long baseline neutrino experiment
(A. Konaka, TRIUMF)

The T2K long baseline neutrino experiment has been approved by the Japanese government, and the neutrino beam line construction started in April, 2004. Sending a beam from the new 1 MW class accelerator at J-PARC (Japan Proton Accelerator Research Complex) to the existing water Čerenkov detector, Super-Kamiokande, it aims at determining the lepton mixing angle θ_{13} and greatly improving the precision on the mixing parameters Δm_{23}^2 and θ_{23}. The commissioning of the J-PARC accelerator is scheduled for 2008 and the first T2K neutrino beam is expected in the beginning of 2009.

The T2K collaboration in Canada consists of accelerator scientists at TRIUMF and physicists and students across Canada from TRIUMF, Alberta, UBC, Carleton, Montreal, Toronto, Victoria, and York University. The Canadian group has been involved in T2K from the very beginning stages of the conceptual design. In particular, we introduced essential design concepts, such as the idea of the $\nu_\mu \rightarrow \nu_e$ analysis and the narrow band off-axis beam, and contributed to the ac-

celerator beam dynamics study, dual abort/extraction kicker design, and the combined function magnet design.

The neutrino beam is produced by a high intensity proton beam hitting the target to produce pions, which decay in the following decay volume to produce neutrinos ($\pi \rightarrow \mu\nu$). The T2K neutrino beam line is the first megawatt beam line. One of its most challenging areas is the target station where a large fraction of the megawatt energy is released. Full remote maintenance is required for the target and the focusing horn magnets. Although the T2K target station is much larger, the structure is very similar to the ISAC target station. The T2K beam line construction group has visited TRIUMF to learn from it, and the TRIUMF experts have contributed to reviewing the conceptual design of the target station. Detailed engineering design of the target station will take place in the next couple of years, and TRIUMF is expected to contribute to the remote handling designs under the new TRIUMF Five-Year Plan. An accelerator contribution, namely the beam damper system in the main ring, is also expected in the Five-Year Plan.

Monitoring the neutrino source is essential in understanding and controlling the neutrino beam. It is done in three places: the primary proton beam monitor, a muon monitor at the beam dump, and a neutrino monitor (on-axis neutrino detector). The Canadian group is in charge of the proton beam profile monitor right in front of the target (target monitor) based on an optical transition radiation (OTR) detector. OTR detectors have been used for electron machines and recently adopted for proton machines at CERN and FNAL. An OTR would likely be the only profile monitor that would work under the extremely high radiation environment in front of the target.

The neutrino oscillations are observed by measuring the neutrino flux in the far detector, Super-Kamiokande, compared with that in an off-axis near detector which is placed in the same direction as the far detector. The off-axis near detector (see Fig. 20)
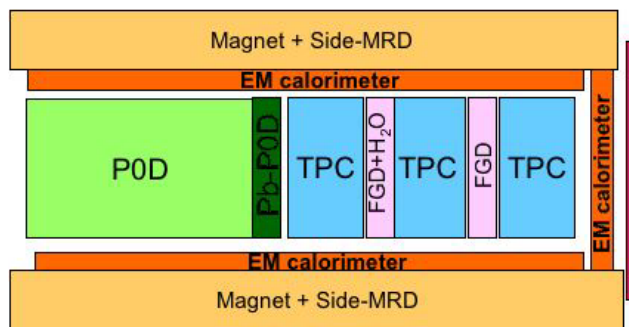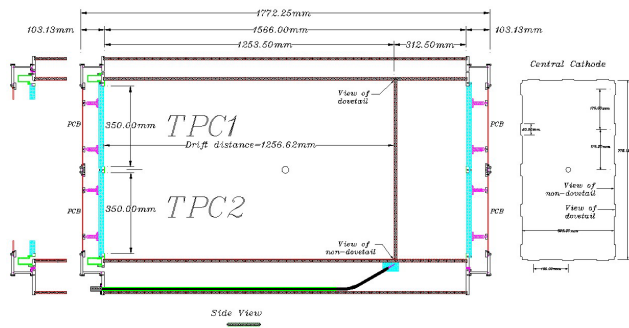

Fig. 21. Prototype design of the TPC.

consists of fine grained calorimeters (FGD, P0D) and time projection chambers (TPC), and an electromagnetic calorimeter (Ecal), which are placed inside the large dipole magnet used for the UA1 experiment at CERN.

The Canadian group is in charge of the TPCs and two FGDs, one based on plastic scintillator and the other based on water-soluble scintillator. There will be three TPCs, each of which is $2.4\,\text{m} \times 2.4\,\text{m} \times 0.9\,\text{m}$ with an electron drift distance of $1.2\,\text{m}$ (see Fig. 21). A leading candidate for signal readout is the gas electron multiplier (GEM), which has been studied for linear collider detector R&D.

The FGD (Fig. 22) serves as the neutrino target mass. The required granularity is about $1\,\text{cm} \times 1\,\text{cm}$ in cross section to be able to detect recoil protons from the quasi-elastic scattering process $\nu_\mu n \rightarrow \mu^- p$.

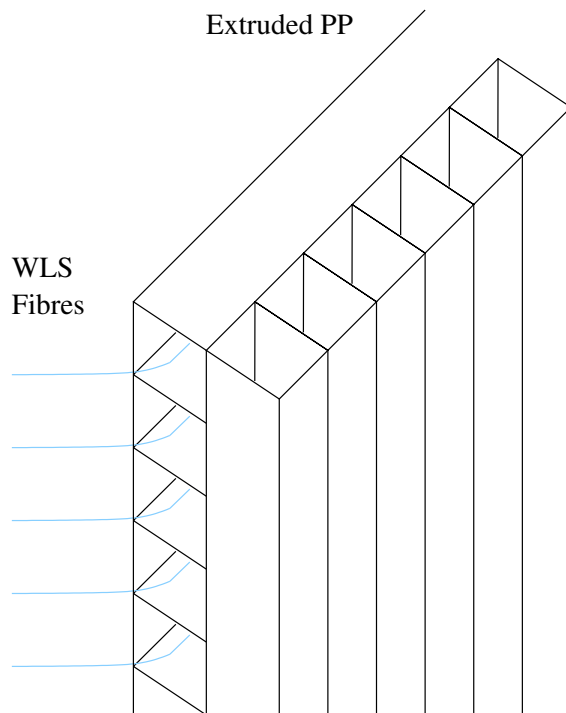Fig. 20. Conceptual schematics of off-axis near detector.

Fig. 22. Schematic view of the water-based FGD.

Because the far detector is water, a scintillator with high water content is desired. We have achieved a water content of 70% with a water-soluble scintillator (Quicksafe A) by adding surfactants. The water-mixed scintillator is contained in polypropylene corrugated plastic sheets with a cell size of $1\,\text{cm} \times 1\,\text{cm}$ and the emitted light is read out by wavelength shifting fibres.

A leading candidate for the FGD photosensor is a multipixel Geiger-mode avalanche photodiode (silicon photomultiplier). R&D for the scintillator and photosensor is under way.

The design of the manipulator for the optical calibration of the 1 kton front detector in the ongoing K2K experiment was completed, and construction begun. The manipulator will be deployed in the coming year.

R&D for the Canadian contributions to the T2K detector, TPC, FGD, and OTR, as well as Canadian participation in K2K, has been funded by NSERC.

Sudbury Neutrino Observatory
(R. Helmer, TRIUMF)

As noted in last year's Annual Report, discrete ^{3}He counters were installed in the heavy water during 2003. Unfortunately, there were several problem strings of counters and it wasn't until the summer (2004) that these were all resolved well enough to begin routine operation. Commissioning continued until late November, at which time a period of running began with the data set open to full analysis. At the end of the year this mode of operation ended and full production running, including a blindness scheme for analysis of the data, is to begin at the start of 2005.

The upgraded glove box, referred to in last year's report, was installed in June. The analysis of the first part of the salt data, also referred to in last year's report, was published [Ahmed *et al.*, Phys. Rev. Lett. **92**, 181301 (2004)]. Meanwhile, analysis has progressed on the full salt data set, with publication expected early in 2005.

Two other papers were published by the collaboration during 2004. In one [Ahmed *et al.*, *ibid.* 102004 (2004)], constraints were placed on nucleon decay into "invisible" modes, e.g. $n \rightarrow 3\nu$. The analysis was based on a search for γ-rays from the de-excitation of the residual nucleus that would result from the disappearance of either a proton or a neutron from ^{16}O. A limit of $\tau_{\text{inv}} > 2 \times 10^{29}$ years was obtained at 90% confidence for either decay mode, an order of magnitude more stringent than previous constraints on invisible proton decay modes and 400 times more stringent than similar neutron modes.

The other published result [Aharmim *et al.*, Phys. Rev. **D70**, 09301 (2004)] concerned a search for electron antineutrinos. These could possibly arise in the solar flux or from neutron induced fission of naturally occurring elements. It has been suggested that antineutrinos could be produced either by spin flavour precession in the magnetic field of the sun or by decay of a heavier neutrino mass eigenstate into a lighter antineutrino. The signal is distinctive, $\overline{\nu}_e + d \rightarrow e^+ + n + n - 4.03$ MeV, and the triple coincidence permits a search with low background. In the case of $\overline{\nu}_e$s from nuclear fission, the positron energies from the charged current interaction are below the threshold for detection in an analysis which includes the positron, but it is possible to search for these events nonetheless by looking only at two-neutron coincidences. The latter analysis includes (e^+, n) coincidences, as it is not possible to separate neutron from positron signals on an event by event basis. Hence these signals add to the triple coincidence detection of solar $\overline{\nu}_e$, and in fact are 10 times more likely to be detected than either (n, n) or (e^+, n, n) coincidences. The time coincidence window was set to 150 ms to optimize the sensitivity to 2-fold coincidences in the presence of a background of accidental coincidences. The total background from all sources to these signals was estimated to be $1.7^{+0.9}_{-0.5}$ coincidences.

Two candidate events were observed – one 3-fold and one 2-fold coincidence. Integral limits on the $\overline{\nu}_e$ flux in the energy ranges from 4–14.8 MeV and below 8 MeV were derived from these events, and spectrally independent differential limits were also obtained. The limit from 4–14.8 MeV shows that less than 0.81% of the solar ν_e flux converts to $\overline{\nu}_e$ (90% C.L.), and is comparable to, and consistent with, a similar limit obtained by Super-Kamiokande. The limit obtained for neutron induced fission $\overline{\nu}_e$s in the energy range 4–8 MeV (2.0×10^6 cm^{-2}s^{-1} at 90% C.L.) is consistent with, but not as constraining as, a similar limit from KamLAND. Similarly, limits on neutrino decay were obtained that were consistent with KamLAND results, but again the SNO results were not as constraining.

The ^{8}Li source has been sent to TRIUMF for refurbishing before it is used again for calibration. The inside of the spherical source chamber was painted several years ago to enhance the light yield from ^{4}He scintillation events, and it is feared some of the paint has flaked off.

TJNAF Experiment 00-006
Measurement of the flavour singlet form factors of the proton ($G\emptyset$)
(W.T.H. van Oers, Manitoba)

The structure of the nucleon at low energies in terms of the quark and gluon degrees of freedom is not well understood. The $G\emptyset$ experiment is to measure two proton ground state matrix elements which

are sensitive to point-like strange quarks and hence to the quark-antiquark sea in the proton. The matrix elements of interest are the elastic scattering vector weak neutral current charge and magnetic form factors, G_E^Z and G_M^Z, respectively. These can be extracted from a set of parity-violating electron-proton scattering measurements. If one assumes a relationship between the proton and neutron structure in that the proton and neutron differ only by the interchange of up and down quarks, i.e., isospin symmetry, the strange quark (as well as the up and down quark) contribution to the charge and magnetic form factors of the nucleon can be determined. This would result from taking appropriate linear combinations of the weak neutral form factors and their electromagnetic counterparts.

Determinations of both the charge and magnetic strange quark form factors are of fundamental interest, as these would constitute the first direct evidence of the quark sea in low energy observables. It is the objective of the $G\emptyset$ experiment to determine these contributions to the proton form factors at the few per cent level. Observations at high energy suggest that the strange quarks carry about half as much momentum as the up and down quarks in the sea. It is important to determine both the role of the quark sea and the relevance of strange quarks at low energy where there are voids in understanding the theory of the strong interaction (quantum chromo dynamics, QCD). Even if the strange quark contributions do not amount to the level of sensitivity of the experiment, upper limit determinations at this level are as valuable as non-zero results. The matrix elements, G_E^Z and G_M^Z, are also relevant to discussions of the Ellis-Jaffe sum rule and the pion-nucleon sigma term; there is uncertainty in both of these about the strange quark contributions. The $G\emptyset$ experiment will allow the determination of the strange contributions to the proton charge and magnetic form factors in a much more straightforward manner than is possible with regard to the corresponding observables in the above two deduced relations.

$$A_z = (1/P)\frac{[\sigma^+(\theta) - \sigma^-(\theta)]}{[\sigma^+(\theta) + \sigma^-(\theta)]}$$

where P is the polarization of the incident electron beam and the $+$ and $-$ signs indicate the helicity state. Making pairs of measurements at forward and backward angles will allow the separation of G_E^Z and G_M^Z. Predicted longitudinal analyzing powers range from about $(-3$ to $-35) \times 10^{-6}$; it is planned to measure the longitudinal analyzing powers with statistical uncertainties of $\Delta A/A = 5\%$ and systematic uncertainties related to helicity correlated effects of $\Delta A/A \leq 2.5 \times 10^{-7}$.

The heart of the $G\emptyset$ detection system is a spectrometer which consists of an eight-sector toroidal magnet, with an array of scintillation detectors located at the focal surface of each octant and, for the backward angle mode, additional arrays of scintillation detectors and a Čerenkov detector located near the magnet cryostat exit window of each octant. In the first phase of the experiment longitudinal analyzing powers have been measured concurrently at several values of the momentum transfer in the range $0.1 \leq Q^2 \leq 1.0$ GeV^2. It must be realized that the length of the experiment is in part governed by making rather elaborate control measurements to determine the corrections that have to be made to the measured asymmetries and to assess systematic errors. In the second phase of the experiment each subsequent backward angle analyzing power measurement would require one month of continuous running time. The results of the SAMPLE experiment at the MIT-Bates laboratory have shown the importance of measuring the axial form factor corrections. Therefore, companion measurements of quasi-elastic scattering from deuterium will also be made at the backward angles. With these measurements, the effective axial current of the nucleon will also be determined. This current includes effects from the effective axial coupling of the photon to the nucleon or anapole moment, which are relevant also in other processes, e.g. parity violating Moller scattering and atomic parity violation.

The past year culminated in a very successful datataking run completing the first phase, forward angle mode, of the $G\emptyset$ experiment (December, 2003 to May, 2004). Preliminary results have been presented at the Gordon Research Conference on Photonuclear Reactions (Tilton, NH, August 1–6, 2004) and at the DNP Fall Meeting (October 28–30, 2004). Considerable progress has also been made in the design, prototyping, fabrication, testing, and installation of critical components for the second phase, backward angle mode, of the experiment, in particular the cryostat exit detectors, the aerogel Čerenkov detectors, and the support structure for these. The Canadian contributions to these efforts have been significant.

An enumeration of the various Canadian contributions to the $G\emptyset$ experiment is given below. As well, a brief description of the recently completed $G\emptyset$ forward angle run is provided, followed by a summary of the progress made in preparing for the second-phase backward angle measurement.

Canadian contributions

The Canadian members of the $G\emptyset$ collaboration, based at the Universities of Manitoba, Northern British Columbia, and TRIUMF, have made the following contributions:

1. Develop and produce specialized photomultiplier tube bases for the focal plane detector arrays;
2. Design, build, and commission an automated magnetic field measuring ("magnetic verification") apparatus complete with its own data acquisition system;
3. Prototype and fabricate the cryostat exit detector arrays for the backward angle measurements;
4. Prototype and fabricate (together with the Grenoble group) the aerogel Čerenkov arrays for background rejection in the backward angle measurements;
5. Design the support structure for the aerogel Čerenkov and cryostat exit detector arrays;
6. Coordinate the implementation of TJNAF built beam monitors and control apparatus with TRIUMF built parity electronics.

The forward angle run

The $G\emptyset$ experiment ran in forward angle mode from December 1, 2003 to May 9, 2004. The run was originally scheduled to begin in mid October, but September's hurricane Isabel caused a major power outage at Jefferson Lab and delayed the startup by six weeks. The periods in December and January were devoted to engineering runs in preparation for 13 weeks of production running from February 9 to May 9, 2004. University of Manitoba personnel staffed a total of approximately 30 person-weeks of shifts. The experiment accumulated approximately 10 Tbytes of good production data corresponding to 94 Coulombs of beam on the liquid hydrogen target.

To extract the final physics asymmetry, the data must first be corrected for deadtime, helicity correlated beam properties, leakage, and background under the elastic peak.

A blind data analysis is now under way. Preliminary blinded data were presented in August at the Gordon Photonuclear Conference.

An overview of the $G\emptyset$ equipment is shown in Fig. 23. The 3 GeV electron beam enters from the lower right where it first encounters the $G\emptyset$ beam monitors. Continuing from right to left, one sees the liquid hydrogen target service module, the eight-sector superconducting magnet system (SMS), and the focal plane detectors mounted in the eight sector "Ferris wheel" structure between the SMS and the green wall. The principle of the forward angle measurement is illustrated in Fig. 24. Longitudinally polarized electrons scatter from the liquid hydrogen target, and the spectrometer accepts recoil protons in the angular range $62°$ to $78°$ (corresponding to $15°$ to $5°$ electrons). The spectrometer magnet is designed so that protons corresponding to a given momentum transfer (Q^2) are
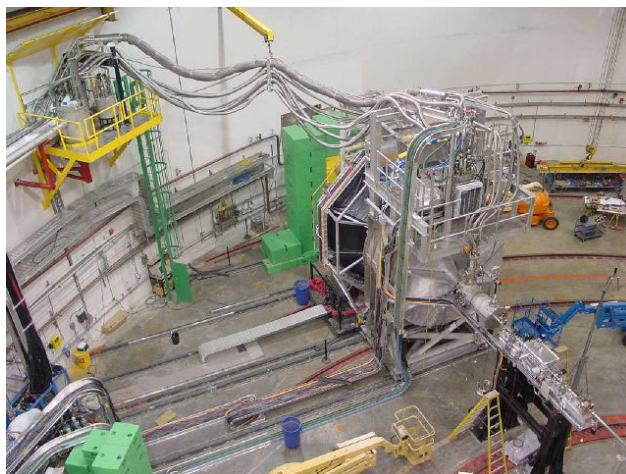

Fig. 23. The $G\emptyset$ apparatus installed in Hall C at Jefferson Lab. The beam enters from the lower right. From right to left, we see the $G\emptyset$ beam monitoring girder, the LH_2 target service module, the 8-sector superconducting magnet, the detector Ferris wheel, and the green shielding wall.
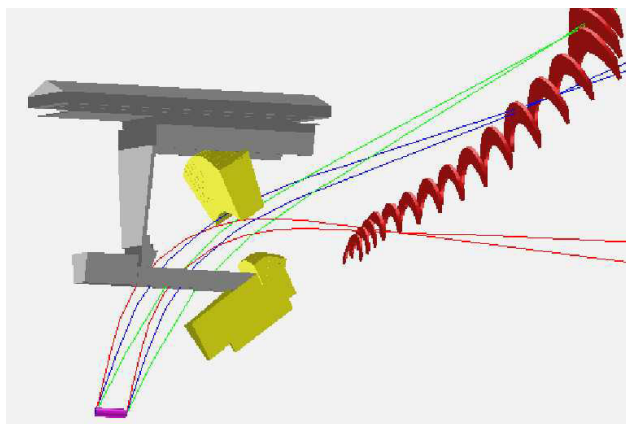

Fig. 24. Principle of the forward angle measurement. The 3 GeV longitudinally polarized electron beam enters the 20 cm liquid hydrogen target from the left. Recoil protons in the angular range $62°$ to $78°$ are deflected to the focal plane detectors, which are arranged along contours of constant Q^2. The magnet sorts the protons by Q^2, regardless of where in the target they originate. Q^2 from 0.16 to $1.0 \, (\text{GeV}/c)^2$ can be measured with one magnet setting.

directed to a specific focal plane detector regardless of where in the target they originate. Q^2 from 0.16 to $1.0 \, (\text{GeV}/c)^2$ can be measured with one magnet setting. The experiment uses a beam time structure with beam bunches 32 ns apart. This is 16 times the usual Jefferson Lab spacing of 2 ns, and permits the protons from elastic scattering to be separated by time of flight from pions and inelastic protons.

Helicity correlated beam properties The helicity of the longitudinally polarized electron beam was selected every $1/30$ second. The spin states were chosen in quartets, either $+--+$ or $-++-$, the first state of

Table V. Helicity correlated beam properties for the February–May production run compared to $G\emptyset$ specifications. These must be multiplied by the sensitivity to these quantities to give the false signal. In the end, the false asymmetry from helicity correlated beam parameters was <0.01 ppm.

Beam parameter	Achieved	Specification
Charge asymmetry	-0.3 ± 0.3 ppm	1 ppm
x position difference	6 ± 4 nm	20 nm
y position difference	8 ± 4 nm	20 nm
x angle difference	2 ± 0.3 nrad	2 nrad
y angle difference	3 ± 0.5 nrad	2 nrad
Energy difference	58 ± 4 eV	75 eV

the quartet being chosen at random. Ideally, no other beam property would be affected, but in practice small changes in beam properties other than helicity occur. Thanks to good design practices such as cylindrical symmetry, the sensitivity of the experiment to helicity correlated beam properties was very small. Nevertheless, it was necessary to constantly monitor helicity correlated beam properties and to correct for the resultant false asymmetry. Table V shows the helicity correlated beam parameters for the forward angle data. Charge and position feedback were used. The helicity correlated beam properties are all very small and, taken together, produced a false asymmetry <0.01 ppm.

Leakage An unanticipated effect was the leakage of beam from the Hall A and B lasers. Hall A and B beams are 499 MHz, but the Hall C beam is 31 MHz. Unfortunately, the beam current monitors which are used to measure the charge asymmetry measure all the time and respond to the total A+B+C beam, whereas the $G\emptyset$ time-of-flight cut sees only the 31 MHz beam. This meant that the correction for charge asymmetry was not right. The situation is illustrated in Fig. 25. We were able to measure the effect by looking in a "forbidden region" of the TOF spectrum where the signal could not come from the $G\emptyset$, 32 ns spaced beam bursts. The leakage was typically 50 nA (c.f. 40 μA Hall C) with 340 ppm charge asymmetry. Corrections were made for the effects of beam leakage. The leakage correction is estimated to contribute ~ 0.1 ppm systematic uncertainty.

Background The measured asymmetry can be written as a weighted sum of the true elastic asymmetry and the asymmetry of the background.

$$A_{\text{meas}} = \frac{A_{el} + f_{\text{back}} A_{\text{back}}}{1 + f_{\text{back}}} .$$

To correct for the background, we must know both the background fraction, f, and the asymmetry, A_{back}, under the elastic peak.
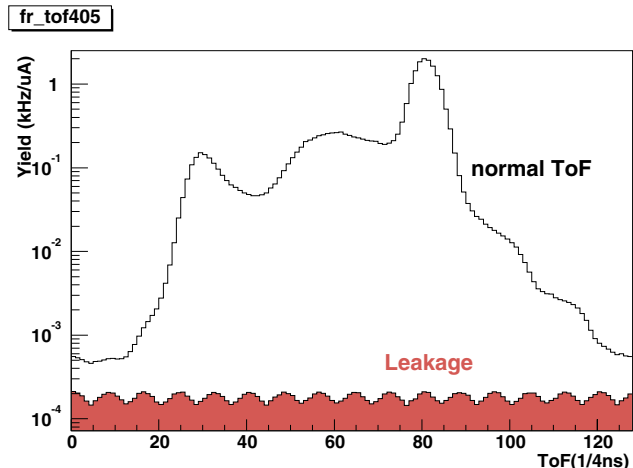

Fig. 25. Contamination of $G\emptyset$ spectra by leakage beam. Some beam from the Hall A and B lasers was found to be leaking into Hall C. The leakage beam was small, about 50 nA compared to the $G\emptyset$ 40 μA main beam, and had the 499 MHz time structure of Halls A and B rather than the 31 MHz Hall C beam.

Following the 2002–2003 engineering run, the target exit window was thinned from 11 mil to 3 mil, which reduced the background under the elastic peak by almost a factor of 2. To better understand the remaining background, an insertable tungsten radiator and insertable dummy entrance and exit windows were provided. Figure 26 shows window backgrounds measured in the 2003–2004 run. In addition to these backgrounds, backgrounds from inelastic LH_2 processes must be taken into account. Using both the measured backgrounds and the results of Monte Carlo simulation, the background fraction can be determined. The fractions were found to vary from about 10% to 40% depending on detector number.
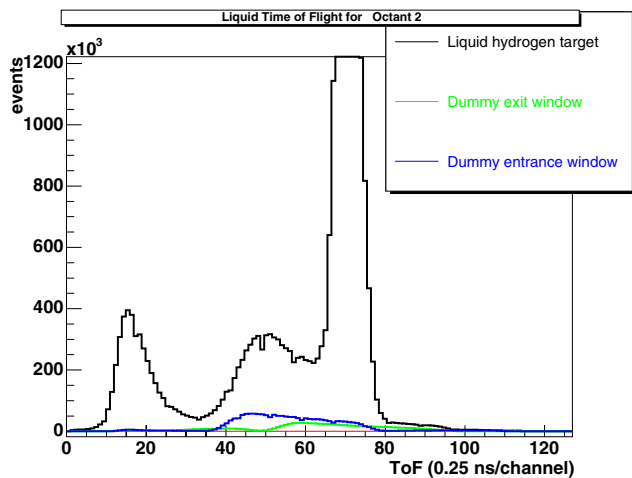

Fig. 26. Estimation of background from entrance and exit widows. The dummy window data have been scaled by charge, thickness and photon flux to match reality in the actual cryogenic cell.
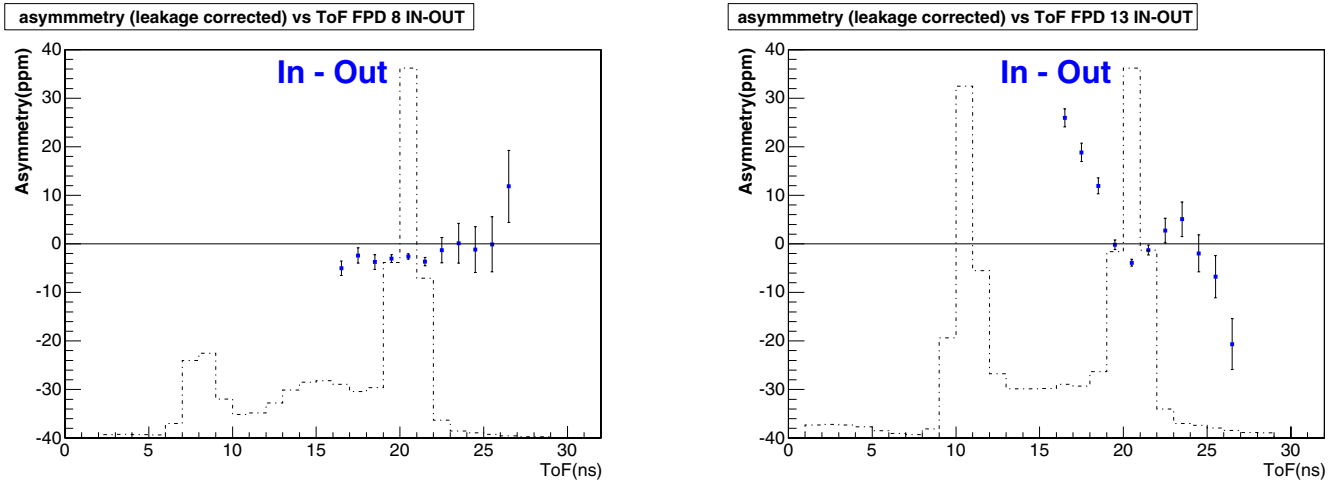
Fig. 27. Estimation of background asymmetry under the peak. The asymmetry is measured on each side of the elastic peak and an interpolation is made. The background correction is more difficult for the higher numbered (higher Q^2) detectors.

Figure 27 shows how the background asymmetry under the peak is estimated by measuring the asymmetry on each side of the peak and interpolating. This method works well for the lower numbered detectors.

Monte Carlo simulations, and investigations of alternative background fitting methods are continuing to make sure that backgrounds are properly understood. The systematic uncertainty in the final result is expected to be dominated by background corrections.

Preliminary data To avoid unintentional bias in the analysis, a blinding factor of from 0.075 to 1.25 has been applied. This is done in such a way as to have the same effect as the wrong beam polarization. Figure 28
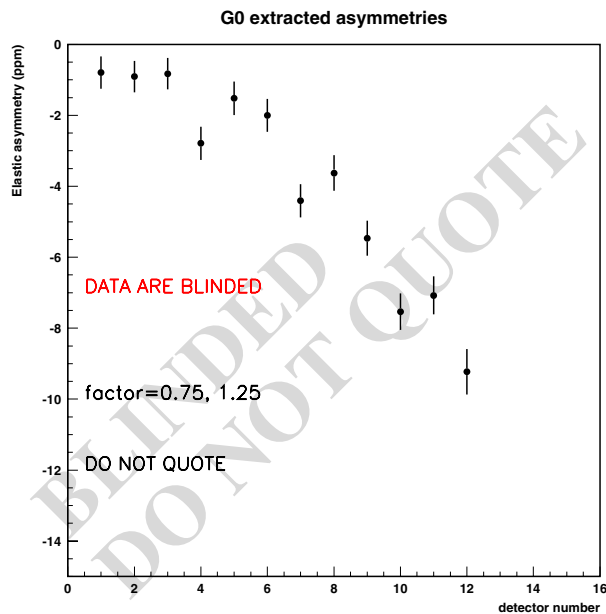

Fig. 28. Preliminary data. The data are not fully corrected and are blinded by an as yet undisclosed factor of 0.75 to 1.25. No data are shown for the highest detectors because the background corrections are not complete.

shows the data presented at the Gordon Photonuclear Conference in August. The background corrections are still being studied for the highest detector numbers, so these data are not included.

Backward angles

Backward angle running involves detecting electrons at 110°. While at forward angles there was a large variation of Q^2 over the $G\emptyset$ acceptance, in the backward angle configuration the kinematics are such that there is very little variation of Q^2 with angle. For this reason the experiment plans separate runs at beam energies of 424, 576, and 799 MeV, corresponding to Q^2 = 0.3, 0.5, and 0.8 $(\text{GeV}/c)^2$. This will be done for both LH$_2$ and LD$_2$ targets for a total of 6 runs of 700 hours each. The back angle run will use the normal Jefferson Lab 2 ns bunch spacing. We also hope to raise the beam current to 80 μA.

Now that the forward angle data-taking is complete. The experiment is being reconfigured in backward angle mode. The detector Ferris wheel and spectrometer magnet were turned around in August.

The backward angle running also requires some additional detectors. The cyrostat exit detectors (CED) are scintillators that will be used to separate elastic and inelastic electrons. These detectors have been built by Manitoba scientists in collabration with TRIUMF and are now at Jefferson Lab. To reject pion background (primarily in the LD$_2$ target run), aerogel Čerenkov detectors have been built by the French and Manitoba/TRIUMF/UNBC collaborators and were delivered to Jefferson Lab in the fall.

Progress for the backward angle run

Cryostat exit detectors For the backward angle second phase of the $G\emptyset$ experiment, the addition of a second array of scintillation detectors, located near the
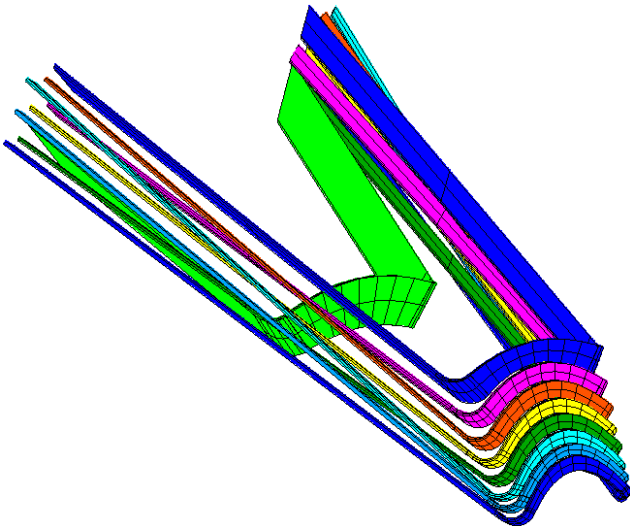
Fig. 29. Layout of a cryostat exit detector (CED) array for a single octant.

spectrometer cryostat exit windows, will be required in order to separate the elastic and inelastically scattered electrons. The geometry of these cryostat exit detector (CED) arrays (see Fig. 29) has been studied in detail and a reference design was completed. With the resident expertise at TRIUMF in producing high quality scintillation detectors and lightguides, the Canadian subgroup was asked to play the lead role in the prototyping and production of the CEDs. A set of prototype CEDs was built at TRIUMF and delivered to the $G\emptyset$ collaboration for studies with cosmic rays. Results from these studies showed that the reference design and the prototype detectors met the specification requirements for these arrays. Production of a full set of CED prototypes was then completed at TRIUMF to aid in the design of the CED support structure. After finalizing the CED design, construction of the "production" versions of the CED arrays began. Fabrication of the CED scintillators for all 8 octants was completed and delivery was made to TJNAF in late 2001, and fabrication of the special helical-bent lightguides began in 2002. In order to achieve the unique helical bend required in the $G\emptyset$ backangle geometry, customized bending jigs were designed and constructed at TRIUMF and tested on a first set of prototype CED lightguides. Production of a full set of lightguides for the first CED octant was completed with delivery to TJNAF in 2003, where they underwent further quality-control tests. Production of the lightguides for all 8 octants was completed with delivery to TJNAF in early 2004. Presently, the CED arrays are being assembled and tested on special support frames, which were designed at TRIUMF. These support frames (the mini Ferris wheel) will be mounted onto the existing $G\emptyset$ detector support structure in 2005. The CEDs will make use of the same types of photomultiplier tubes and specialized TRIUMF/$G\emptyset$ bases as the focal plane detectors.

Aerogel Čerenkov detectors Monte Carlo simulation results have shown that backgrounds from negative pions will be problematic for the second phase backward angle measurements involving the deuterium target. The $G\emptyset$ Simulation subgroup focused on characterizing this π^- background and provided options regarding the design of an additional set of detectors to reject the background pions. The $G\emptyset$ Canadian and French (Grenoble) subgroups have been asked to jointly undertake the prototyping and construction of this crucial set of detectors, which will be made up of an array of aerogel Čerenkov counters. Much effort went into the design of this detector array and a conceptual design was evolved into a first prototype at TRIUMF.

In October–November, 2003 a last run was performed with the prototype box to investigate the effect of variations in box geometry and the effect of pulling back the PMTs to a more realistic position for the purpose of magnetic shielding. The final design of the Čerenkov detector was completed, allowing for more realistic shielding of the PMTs and better matching of the acceptance to the distribution of scattered electrons. Four such detectors were built in the TRIUMF Machine Shop.

In addition, newly designed PMT housings were constructed for the 16 PMTs. Tests were also done within a large C-magnet on the requirements and effect of the magnetic shielding.

Three of the four boxes were sent to Jefferson Lab; one was kept at TRIUMF for later tests. The Jefferson Lab boxes were loaded with aerogel tiles, including cut angled pieces at the edges. The retention system consisting of a harp of wire-chamber wires threaded onto an insertable frame was assembled and shown to function properly (see Figs. 30 and 31). A test was also conducted to show that the Čerenkov detectors would fit onto the support frames.

At TRIUMF, further tests are planned in the M11 beam line to calibrate the light output with $\pi/\mu/e$ beams, using the final production detector. Following these tests, this last detector will be delivered to Jefferson Lab.

Backangle support structure Considerable effort has gone into the engineering design of a support structure for the $G\emptyset$ Čerenkov and CED arrays. Although the Canadian subgroup was initially responsible only for the design of the Čerenkov support structure, it was soon realized that the CED support structure would be closely coupled to the former due to the physical proximity of the two detector subsystems. As such, an integrated design for the two detector subsystems was
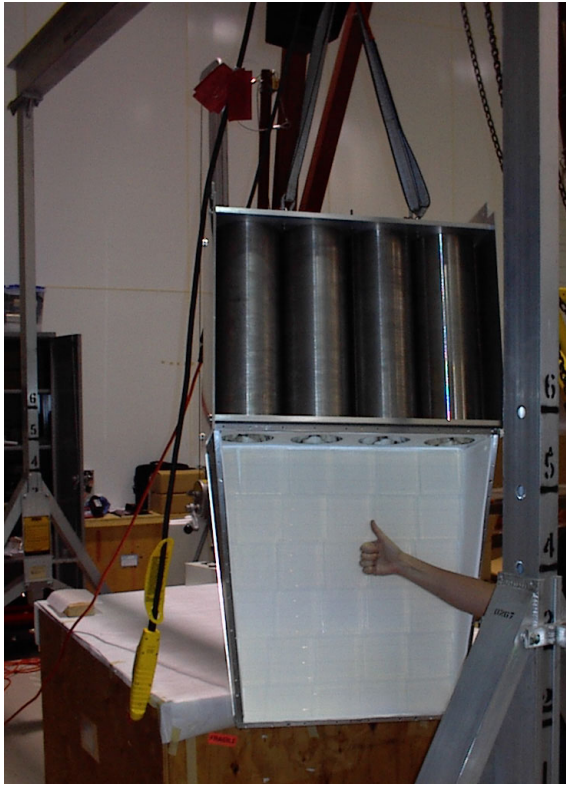
Fig. 30. The new $G\emptyset$ production version of the aerogel Čerenkov box after arrival at Jefferson Lab. The box is full of aerogel with retainer in place.

Fig. 31. The new boxes and PMT housings after arrival at Jefferson Lab and ready to go.

pursued. The support structure centres around the use of prefabricated aluminum extrusions from Bosch because of their strength, versatility, and relatively low costs. A series of detailed finite-element analysis studies was carried out at TRIUMF, using the program ANSYS, to identify potential problems and to optimize the strength and cost of the support structure. The design consists of a second Ferris wheel type support structure, which will couple to the existing FPD support structure (also a Ferris wheel type design) and to the linear rails on the existing $G\emptyset$ detector platform. A conceptual illustration of the $G\emptyset$ backward angle configuration is shown in Fig. 32, with the superconducting magnet, the 3 detector arrays (FPD, CED, Čerenkov) in each of the 8 sectors, and their respective support structures.

In the spring of 2003, the parts for a single octant of the support frame were procured and successfully assembled at TJNAF (see Fig. 33). As various components of the backward angle detectors arrived at TJNAF over the summer of 2003, work began on a "test assembly" of one octant of the backward angle system to validate the overall design and assembly procedure. In particular, the positions of the CED scintillators had to be accurate to $\pm 2\,\mathrm{mm}$, and the scintillators themselves could only be directly supported by a low-density material. Furthermore, the CED scintillators would have to be glued *in situ* to their respective lightguides and any potential interferences between adjacent detectors would have to be identified and reconciled. An assembly to locate and hold the CED scintillators was designed and built (see Fig. 34). This assembly was constructed from a structural foam material, Rohacell-71, which is light-weight ($\approx 71\,\mathrm{g/cm^3}$) and is easily machinable. To help complete the test assembly,
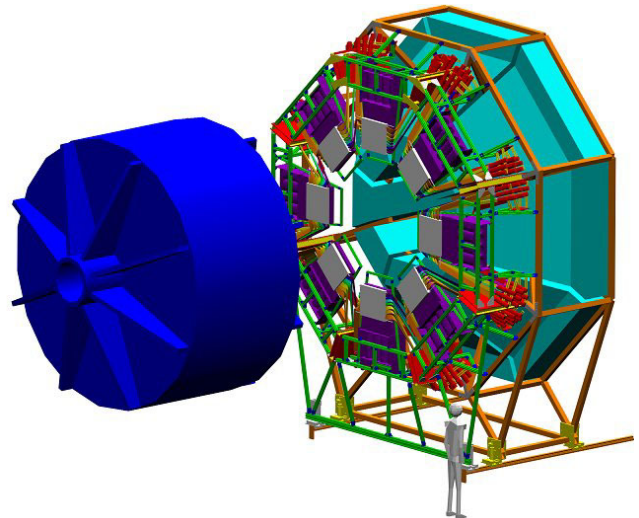

Fig. 32. Conceptual layout of the $G\emptyset$ backward angle configuration.
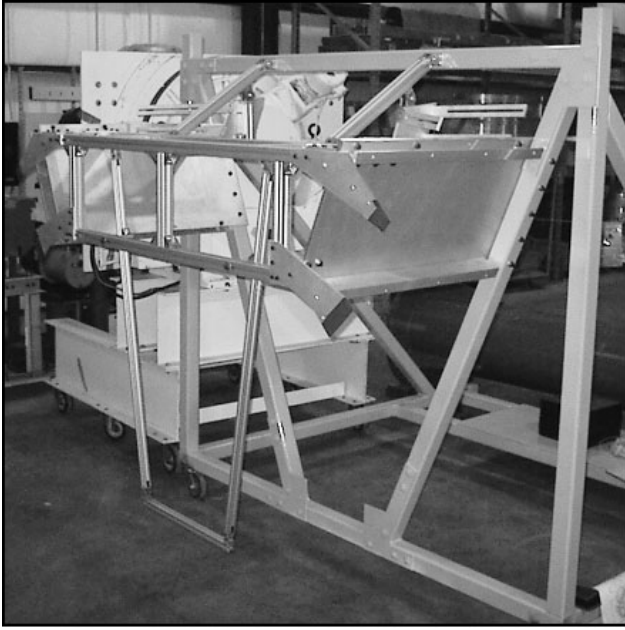
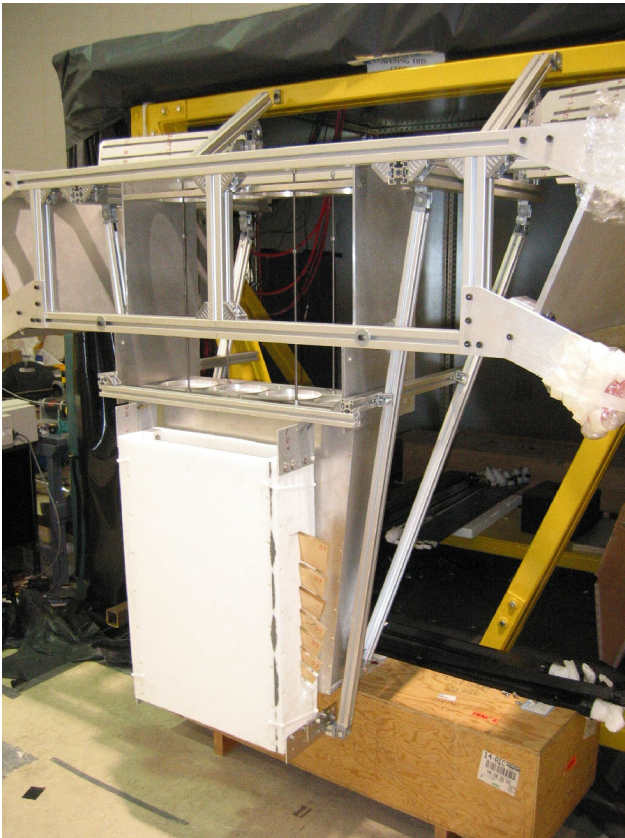Fig. 33. A single octant of the backangle detector support frame.

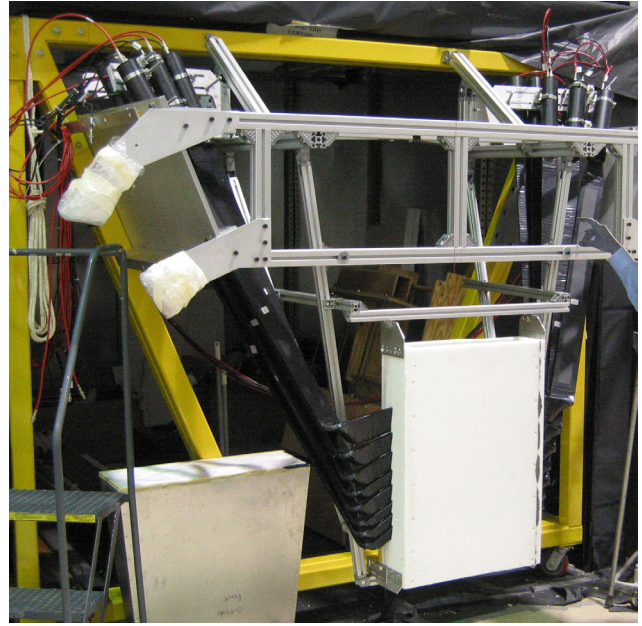Fig. 34. The Rohacell assembly which both positions and supports the CED scintillators.

Fig. 35. The first completed octant of CEDs, assembled *in situ* within its octant support frame.

both the Canadian and French groups supplied mock-up Čerenkov detectors for test mounting in the support structure frame. Both Čerenkov mock-ups were test fitted and met the nominal mechanical design specifications. In late 2003, the test assembly was completed and the overall support frame design was validated.

In the spring of 2004, procurement of parts for the remaining 7 octants of the support structure began. At the same time, final assembly of the first octant of CEDs also began. By late summer, all parts for the CED octant support frames were delivered to Jefferson Lab, and assembly of the remaining octant support frames was well under way. As well, the first octant of CEDs was successfully assembled (see Fig. 35) and a first set of tests, using cosmic rays, was carried out to quantify the light yield in these detectors. Over the fall, efforts focused on completing the assembly of the remaining octant support frames and assembling the CED arrays *in situ* within these frames. Presently, cosmic ray calibrations of the CED arrays are under way and will continue into early 2005.

Future It is expected that set-up of the backward angle configuration will be completed in the fall, 2005, with a first run possible in late 2005.

Canadian subgroup of the $G\emptyset$ collaboration: J. Birchall, W.R. Falk, B. Jasper, Z. Ke, L. Lee, S.A. Page, W.D. Ramsay, G. Rutledge, M.J. Steeds, W.T.H. van Oers (Manitoba); E. Korkmaz, T. Porcelli (UNBC); C.A. Davis (TRIUMF).

TJNAF Experiment 02-020

The Q$_{weak}$ experiment: a search for physics at the TeV scale via a measurement of the proton's weak charge

(S.A. Page, Manitoba)

Introduction

The standard model of electroweak interactions has been confirmed with impressive precision in a variety of experiments, ranging in energies from the eV scale in atomic parity violation to a few hundred GeV in collisions at HERA, LEP, SLC, and the Tevatron.

An essential, but not well tested, prediction of the standard model is the variation of $\sin^2(\theta_W)$ with momentum transfer Q^2, referred to as the "running of $\sin^2(\theta_W)$" (see Fig. 36). Because the radiative corrections which result in the running of $\sin^2(\theta_W)$ can reflect contributions from additional force carriers beyond the standard model, a precision measurement of
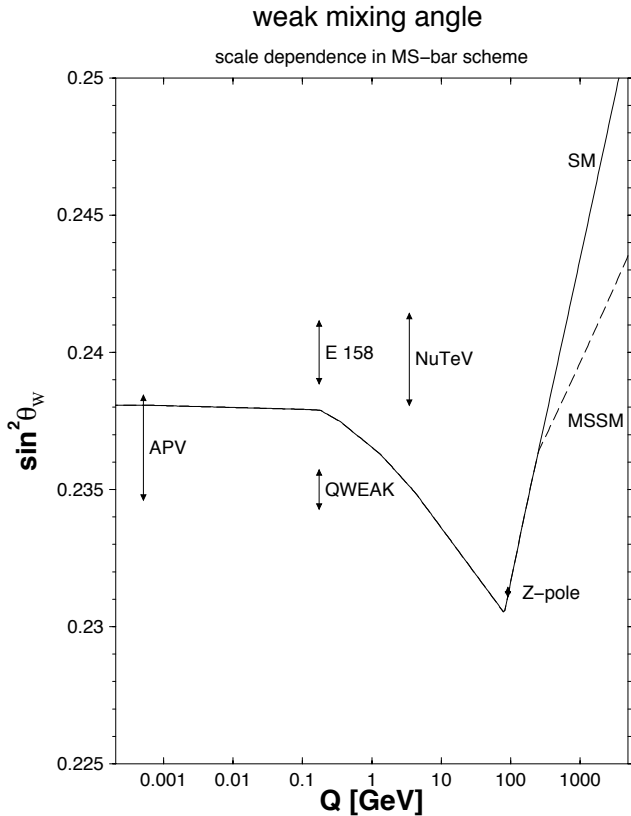

weak mixing angle

scale dependence in MS–bar scheme

Fig. 36. Calculated running of the weak mixing angle in the standard model [Erler *et al.*, Phys. Rev. **D68**, 016006 (2003)]. The data points shown are those from the atomic parity violation experiment on Cs (APV), the SLAC experiment (E158), the FNAL (NuTeV) experiment, and from several leptonic and semi-leptonic experiments at the Z^0 pole. Also shown is the anticipated error bar of the Q$_{weak}$ experiment at Jefferson Lab. Møller and deep inelastic scattering experiments at low Q^2 with different extensions to the standard model may follow the upgrade of CEBAF to 12 GeV.

$\sin^2(\theta_W)$ at low energy will provide a surprisingly sensitive test for new physics.

The very precise measurements at the Z^0 pole (at LEP and SLC) set the overall scale of the running of $\sin^2(\theta_W)$. Shown in Fig. 36 are the precise Z^0 pole point and three other measurements which test the running of $\sin^2(\theta_W)$: an atomic parity violation experiment, the SLAC E158 parity violating electron-electron (Møller scattering) experiment and the Fermilab NuTeV neutrino-nucleus scattering experiment. The Jefferson Lab Q$_{weak}$ experiment will have significantly smaller statistical and systematic errors and has a much cleaner theoretical interpretation than the other low Q^2 measurements. It is worth emphasizing that it is extremely useful to have both the SLAC electron measurement and the Jefferson Lab Q$_{weak}$ proton measurement, as the two are affected differently by different extensions to the standard model. This is illustrated in Fig. 37 [Erler *et al., op. cit.*]. For example, SUSY loops and a 1 TeV Z' would affect both measurements in the same direction, whereas RPV SUSY has effects in opposite directions. Only Q$^p_{weak}$ is sensitive to leptoquarks.

Q$_{weak}$ will measure the parity violating asymmetry in the scattering of longitudinally polarized electrons from protons at very low momentum transfer, $Q^2 = 0.03\,(\text{GeV}/c)^2$, and an energy of $1.12\,\text{GeV}$. Under these conditions, the asymmetry arises almost entirely from the proton's weak charge. The results of earlier electron-proton parity violating experiments will be used to constrain the small corrections from hadronic form factors. A 2200 hour measurement employing $180\,\mu\text{A}$ of 80% polarized beam on a 0.35 m liquid hydrogen target is expected to determine the proton's weak charge with a 4% combined statistical and
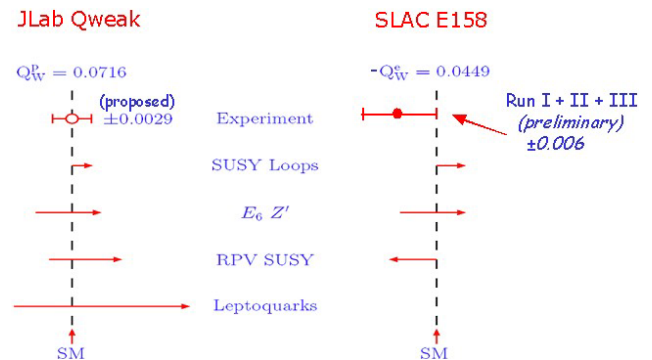

Fig. 37. A comparison of the anticipated error for the Q$_{weak}$ (Q^p_W) experiment and the SLAC E158 (Q^e_W) experiment and the addition of various new physics additions to the standard model that are allowed by fits to existing data at a 95% confidence level. SUSY loops and a 1 TeV Z' would have effects in the same direction for both measurements and could result in evidence for new physics. RPV SUSY has effects in opposite directions. Only Q^p_W is sensitive to leptoquarks, while Q^e_W would serve as a control.

systematic error. A toroidal magnetic field will focus elastically scattered electrons onto a set of eight quartz Čerenkov detectors coupled to photomultiplier tubes, which will be read out in current mode to achieve the high statistical precision required for the measurements. The acceptance averaged asymmetry in the designed experiment is predicted to be -0.3 ppm. This will be measured to $\pm 1.8\%$ statistical and $\pm 1.3\%$ systematic error, leading to the determination of $\sin^2(\theta_W)$ at the 0.3% level. The Canadian group is leading the magnetic spectrometer construction project and are also designing, developing, and fabricating the electronics for the main detector system. Jeff Martin, from the University of Winnipeg, has recently joined the group which now includes members from Winnipeg, Manitoba, UNBC, and TRIUMF. Further responsibilities of the Canadian group are in systematic error evaluations and in beam line monitoring and control apparatus.

The Q$_{weak}$ magnetic spectrometer QTOR

The resistive toroidal magnet with eightfold symmetry has been defined by the magnet working group of physicists and engineers from Jefferson Lab, Louisiana Tech, Manitoba, MIT-Bates, and TRIUMF. The magnet, the coil holders, and the support structure have been designed at MIT-Bates (see Fig. 38). The
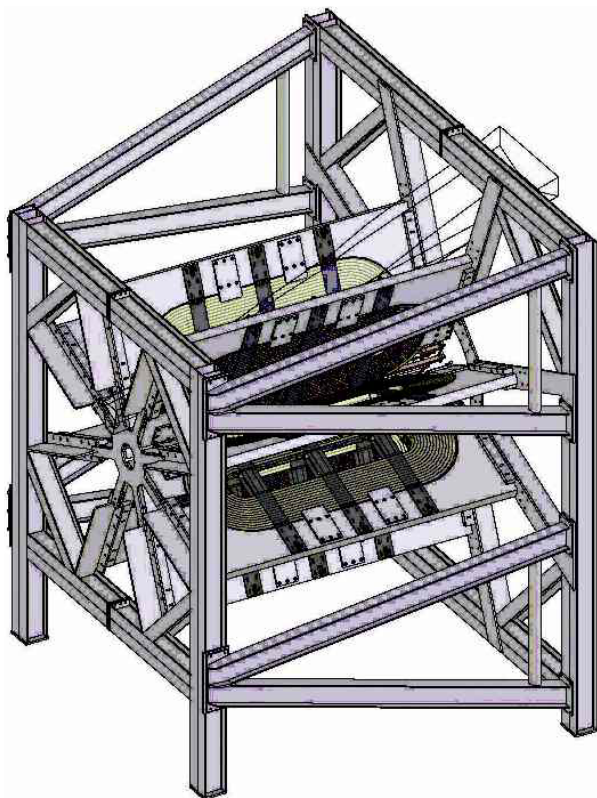

Fig. 38. Three-dimensional view of the Q$_{weak}$ resistive toroidal magnet with its support structure.

copper conductor has been purchased by Jefferson Lab from Phelps-Dodge and delivered to the coil manufacturer. The contract for fabrication of nine coils was awarded to Sigma Phi in Vannes, France. Construction has started and the finished coils are to be delivered to MIT-Bates by the end of July, 2005. The aluminum plate for the coil carriers or holders has been ordered with delivery by March 1, 2005. The current timetable calls for construction of the coil carriers between April 1 and June 30, 2005. A review of the support structure took place in October, 2004. The contract will be awarded in early 2005.

QTOR magnetic field calculations and field mapping

The magnetic field calculation has been updated to reflect information from the latest technical drawings (March, 2004). In this latest design, the coil leads have been modified considerably from the earlier design. The changes result in only very minor differences in the calculated trajectories.

In order to investigate the implications of the latest field calculations and how best to achieve the desired coil placements, sets of ray-trace calculations for a bundle of electron trajectories and absolute field calculations were performed. They were carried out with the coils in their nominal positions and the coils displaced randomly with a normal distribution of $\sigma = 3.5$ mm in the x, y, and z directions, and $\sigma = 4.4$ mrad $(0.25°)$ in rotation. Some sample displacements, in the direction transverse to the bar, are shown in Table VI for sectors 1, 3, 5 and 7. As can be seen, the random coil misalignments generally resulted in unacceptably large displacements of the electron trajectories on the detector bars.

Table VI. Effect of coil misalignment on the position of various rays on the main detector bar. The coil misalignments were chosen randomly from distributions of $\sigma = 3.5$ mm in the x, y, and z directions, and $\sigma = 4.4$ mrad $(0.25°)$ in rotation. Results are shown for octants 1, 3, 5, and 7.

Ray		Transverse displacement on bar (cm)			
θ(deg)	ϕ(deg)	1	3	5	7
6.00	−10.00	0.025	−0.193	−0.018	0.730
6.00	0.00	0.112	−0.160	−0.153	0.959
6.00	10.00	0.049	−0.139	−0.297	1.238
9.00	−10.00	−1.004	−0.287	0.351	0.222
9.00	0.00	−0.872	−0.149	0.265	0.364
9.00	10.00	−1.162	0.106	0.343	0.384
12.00	−10.00	−0.928	−0.630	0.473	0.060
12.00	0.00	−0.896	−0.318	0.369	−0.033
12.00	10.00	−1.175	−0.094	0.564	−0.378

Since the field at any point depends on the total current distribution of all eight coils, measurements of the absolute field are of limited value in ascertaining coil misalignments. They will, however, still be necessary to verify the overall field strength.

Measurements of the zero-crossings of selected field components in the planes at approximately $Z = \pm 180$ cm would permit determination of the coil positions to about 1.5 mm and rotations to about 1.8 mrad $(0.1°)$ Corrections to the coil positions could then be made, reducing to an acceptable level the asymmetries that would be recorded by the detector bars.

The Q_{weak} current mode electronics

The Q_{weak} experiment detects electrons elastically scattered from the liquid hydrogen target at a laboratory angle of $9°$. The experiment will measure the parity-violating difference in scattering cross section for electrons of right-handed and left-handed helicity, expressed as $A_z = (\sigma^+ - \sigma^-)/(\sigma^+ + \sigma^-)$ where σ^+ and σ^- refer to the cross sections for electrons of right-handed and left-handed helicity. It is expected that $A_z \simeq -0.3$ ppm, and it is desired to measure this to a statistical precision of 5×10^{-9} in 2200 hours. To do this requires a count rate of ~ 800 MHz in each of the 8 octants. This is too high for conventional pulse counting techniques, so the experiment will operate in current mode. Custom made electronics for this purpose are being designed and built at TRIUMF.

Figure 39 shows a block diagram of the front end electronics. The current signal from the photomultiplier tube goes to a current to voltage preamplifier followed by a VME based digital signal integrator. These parts, shown in blue on the figure, are the sections to be made at TRIUMF.
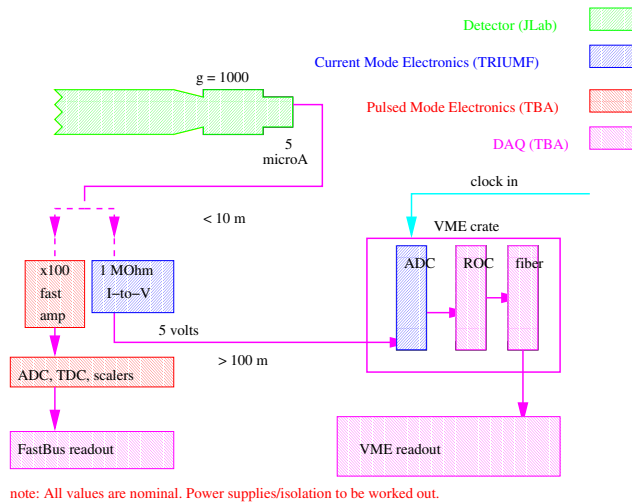

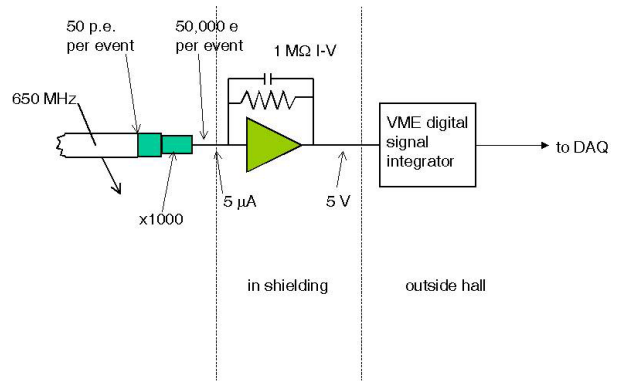Fig. 39. Q_{weak} front end electronics, showing the division of responsibility for different sections.

Fig. 40. Nature of the Q_{weak} signals. The charge quantum of the $5\,\mu$A signal is 50,000 times the electronic charge. The rms shot noise is hence much larger than if the $5\,\mu$A was from a battery.

The nature of the signal Figure 40 indicates how a $5\,\mu$A current signal to the TRIUMF electronics is produced from the high count rate at one of the 8 detectors. It is expected that 50 photoelectrons will be released at the photomultiplier tube (PMT) cathode for a typical event. The gain of the photomultiplier is adjusted to yield $5\,\mu$A at the anode under normal running conditions. In this example, the count rate is 650 MHz; this will require a PMT gain of approximately 1000 (if the count rate is 800 MHz, the current at this gain will be 6.4 μA). The 5 μA signal will be considerably noisier than 5 μA from a battery because it is made from large, 50,000 e charge lumps rather than from single electrons. This "shot noise" is given by $i_n^2 = 2QIB$ $[\mathrm{A}^2]$, where I is the current, Q the charge quantum, and B the equivalent noise bandwidth.

The analogue section of the electronics will be placed in Hall C near the main detectors, but shielded as much as possible from radiation. We hope to reduce the total dose to the analogue electronics to ~ 1 krad. The VME digital signal integrators will be located outside the hall in the Q_{weak} electronics cage.

The custom VME signal integrators must integrate the signal for a time set by the data acquisition and make the result available on the VME bus. The integration time will depend on the spin flip rate. Two schemes have been considered. In the "120 Hz" scheme, each spin state will last $1/30$ s. The current mode electronics will integrate the current over the spin state as four $1/120$ s integrals. The scheme would be insensitive to noise at multiples of the 60 Hz ac line frequency; the 4 times over sampling would let us check if significant line noise was being cancelled by the $1/30$ s integral. In the "1 kHz" scheme, each spin state will only last $1/250$ s and the charge will be digitized as four, 1 ms long, integrals. The argument for the 1 kHz scheme is that it may be difficult to produce a non-boiling liquid hydrogen target to handle 2 kW. Target boiling data

from Hall A indicate that the frequency spectrum of the noise from target boiling is such that bubbling is not seen on a time scale of a few ms.

Method of integration To perform the integration, the VME module divides the integration period, T, into n equal time bins of width Δt and samples the signal at the middle of each bin. The integral is Δt times the sum of the samples.

Analogue bandwidth Integration by this simple method assumes that the sampling rate is high compared to the analogue bandwidth, so that the signal looks like a straight line over one time bin. If this is not the case, either the analogue electronics must be slowed down, or the sampling rate increased. Another important reason to limit the analogue bandwidth is so that signal frequencies higher than half the sampling rate do not "alias" back into the passband. In practice, the digital integrator will have an appropriate sharp cutoff "anti-aliasing" filter built in.

Although, as just explained, we want to restrict the analogue bandwidth, it cannot be made too low. Too low a bandwidth will give too little spread in the individual samples so "least bit" ADC noise will not average out. In addition, the signal we are looking for is a small current signal synchronized with the spin state; an extremely low bandwidth could slow the response to the extent that the electronics would not follow the real signal. Looked at in the time domain, the signal risetime should be fast enough compared to the dead time between spin states that the current is steady on its new value before integration begins.

Noise budget Table VII summarizes the main sources of noise under different running modes. The main noise source during data-taking is shot noise due to the random arrival of electrons at the detectors (i.e. counting statistics). This noise is reduced during beam OFF tests when the charge quantum of the $5\,\mu$A signal is smaller. The numbers in Table VI assume $Q = 50,000\,e$ for beam ON, $Q = 1000\,e$ for LED tests, and $Q = e$ for battery tests. If other sources of noise are small compared to shot noise, then the time to achieve a given statistical precision is proportional to the charge quantum. Beam OFF tests in particular, for which the charge quantum is small, benefit greatly from low electronic noise.

Preamp noise cannot be lower than the thermal noise (Johnson noise) in the 1 MΩ feedback resistor. This white noise, with a density $e_R = 127\,\mathrm{nV}/\sqrt{\mathrm{Hz}}$ at room temperature, appears added to the output voltage. The input resistor also contributes noise, the size of which depends on the capacitance of the input cable. Pspice simulations at TRIUMF indicate around $400\,\mathrm{nV}/\sqrt{\mathrm{Hz}}$. Since the amplifier noise for a modern preamp is several factors of ten below this, we assume the resistor noise dominates. As a fraction of 5 V, this is 0.7 ppm for a $1/120$ s integration or 2 ppm for a $1/1000$ s integration.

For the VME based digital signal integrator being designed at TRIUMF, the noise will depend on details of the design, but will be effectively one or two least significant bits on a 20 bit number. Internally, the integrators will use 16 or 18 bit ADCs (probably 18 bits) with typically 0.5 LSB rms noise that is further reduced by averaging 500 to 1000 samples over the integration period.

Dithering In order for the averaging of ADC "least count" noise to work, the raw signal must be spread over sufficient bins in the input ADC. For example, if the input signal was so quiet that it sat in one bin of the ADC, an artificial noise, or "dithering" would have to be added so that the average of many samples could be taken to determine where in the bin the signal was sitting. The analogue signal will be quieter in the 120 Hz scheme as, due to the slower sampling rate, the bandwidth has to be more limited than in the 1000 Hz scheme. Table VIII summarizes the situation for the worst case of $1/120$ s integration times (assuming an equivalent analogue noise bandwidth of 15.7 kHz ($f_{3db} = 10$ kHz), and a 16 bit ADC operating at half-scale. One sees that there is only a potential problem if beam OFF tests are made with a battery. Only the shot noise contribution is shown. A move to higher bandwidth or 18 bit ADCs, will further reduce any problem. Table IX shows the improvement when the analogue bandwidth is increased to a value appropriate for the 1000 Hz scheme. One can see from the last column that high frequency operation, combined with an 18 bit ADC will ensure that even a quiet signal is spread over sufficient bins.

Required modules In addition to handling the signals from the main detectors, we plan to use TRIUMF electronics for a variety of other instrumentation, for example, luminosity monitors and beam line monitors. Some of these deliver voltage signals and will only need digital integrators while others will need both I-V preamplifiers and digital integrators. Initially, we plan to build 28 dual I-V preamplifiers and 14 octal integrators. This will be adequate to handle the main electronics and essential beam line instrumentation. Depending on funding, it may be possible to supply more modules to upgrade other beam line monitors and to provide spares.

Schedule The following schedule has been adopted:

- 2005 – Preliminary design ready for preamplifiers and integrators. Prototype preamplifier built and tested for radiation hardness.

- 2006 – Prototype VME integrator built and tested.
- 2006 – Design finalized and required modules built
- 2007 – Install and commission detectors and electronics.

List of Q$_{weak}$ collaborators: M.J. Ramsey-Musolf, Caltech; D. Armstrong, T. Averett, J.M. Finn, K.H. Grimm, College of William and Mary; T. Smith, Dartmouth College; C. Keppel, Hampton University; P. Bosted, A. Bruell, R.D. Carlini, S. Chattopadhyay, R. Ent, D.J. Gaskell, A. Lung, D. Mack, S. Majewski, D. Meekins, H. Mkrtchyen, M. Poelker, J. Roche, G.R. Smith, S. Wood, C. Zorn, Jefferson Lab; J.D. Bowman, G. Mitchell, S. Penttila, W.S. Wilburn, Los Alamos National Lab; T. Forest, K. Johnston, N. Simicevic, S. Wells, Louisiana Technical University; J.A. Dunne, Mississippi State University; T. Botto, K. Dow, M. Farkhondeh, W. Franklin, M. Khol, S. Kowalski, Y. Prok, E. Tsentalovich, T. Zwart, MIT; Y. Liang, A.K. Opper, Ohio University; C.A. Davis, J. Doornbos, TRI-UMF; J. Erler, Universidad Nacional Autonoma de Mexico; R. Jones, K. Joo, University of Connecticut; J. Birchall, W.R. Falk, M. Gericke, L. Lee, S.A. Page, W.D. Ramsay, W.T.H. van Oers, University of Manitoba; S. Covrig, F.W. Hersman, M. Holtrop, H. Zhu, University of New Hampshire; E. Korkmaz, T. Porcelli, University of Northern BC; J. Martin, University of Winnipeg; J. Mammei, R. Mammei, N. Morgan, M. Pitt, R. Suleiman, Virginia Polytechnic Institute. Experiment status: in preparation.

Table VII. Noise contributions from different sources.

Condition	Noise on $1/120$ s integral (ppm)	Noise on $1/1000$ s integral (ppm)
Beam ON shot noise	430	1240
Shot noise during LED tests	61	175
Shot noise during battery tests	1.9	5.5
Preamplifier noise	0.7	2.0
Digital integrator noise	1–2	1–2

Table VIII. Number of front end ADC bins covered by the analogue signal for an equivalent noise bandwidth of 15.7 kHz ($f_{3db} = 10$ kHz), appropriate for 8.3 ms integration times. The calculation assumes a 16 bit ADC operating at half of full scale. The last column shows the FWHM with an 18 bit ADC.

Condition	Q (e)	rms noise (mV)	Bins (σ)	Bins (FWHM)	18 bit bins (FWHM)
Beam ON	50,000	36	240	557	2228
LED test	1,000	5	33	79	316
Battery test	1	0.16	1	2.3	9.2

Table IX. Number of front end ADC bins covered by the analogue signal for an equivalent noise bandwidth of 130 kHz ($f_{3db} = 83$ kHz), appropriate for 1.0 ms integration times. As in Table VIII, a 16 bit ADC operating at half scale is assumed. The last column shows the FWHM with an 18 bit ADC.

Condition	Q (e)	rms noise (mV)	Bins (σ)	Bins (FWHM)	18 bit bins (FWHM)
Beam ON	50,000	104	684	1607	6428
LED test	1,000	15	97	227	968
Battery test	1	0.46	3	7	28